

1       **Constraints on the porosity, permeability and porous micro-structure of**  
2               **highly-crystalline andesitic magma during plug formation**

3  
4    Amelia A. Bain\*<sup>1</sup>, Anthony Lamur<sup>2</sup>, Jackie E. Kendrick<sup>2</sup>, Yan Lavallée<sup>2</sup>, Eliza S. Calder<sup>1</sup>,  
5    Joaquín A. Cortés<sup>3</sup>, Ian B. Butler<sup>1</sup>, Gloria Patricia Cortés<sup>4</sup>

6  
7    <sup>1</sup> School of Geosciences, Grant Institute, University of Edinburgh, James Hutton Road,  
8    Edinburgh EH9 3FE, UK

9    <sup>2</sup> School of Environmental Sciences, Jane Herdman Building, University of Liverpool, 4  
10   Brownlow Street, Liverpool L3 5DA, UK

11   <sup>3</sup> Department of Geography, Edge Hill University, St Helens Road, Ormskirk, Lancashire  
12   L39 4QP, UK

13   <sup>4</sup> Servicio Geológico Colombiano, Observatorio Vulcanológico y Sismológico de Manizales,  
14   Manizales, Avenida 12 de Octubre No. 15-47, Caldas, Colombia

15   \* Corresponding author. E-mail address: Amelia.Bain@ed.ac.uk

16

17

18

19

20

21

22

23 **Abstract**

24

25 The development of pore overpressure beneath high-crystallinity, low-permeability magma  
26 plugs is often inferred to be the cause of hazardous vulcanian explosions at many active arc  
27 volcanoes. Using a combination of porosity and permeability measurements and X-ray micro-  
28 tomographic reconstructions of ballistic bombs from the 2004-2010 explosions of Galeras  
29 volcano, Colombia, we document the micro-structural changes of the permeable porous  
30 network in high-crystallinity andesitic magma plugs resulting from natural viscous  
31 densification. Mean pore volumes, mean pore throat areas and the volumetric number density  
32 of connected pores and throats decline as connected porosity and permeability decrease. The  
33 mean pore coordination number and the volumetric number density of disconnected (isolated)  
34 voids also tend to decrease with decreasing porosity and permeability. The variance in pore  
35 volume and throat area decrease as a result of this densification process and tortuosity decreases  
36 slightly, demonstrating that the range of scales of structures performing gas transfer is reduced  
37 and the porous network undergoes viscous re-organisation. The reduction in tortuosity  
38 illustrates how permeability is reduced but maintained to low connected porosities, allowing  
39 plug formation to occur without creating large-scale pore overpressure within the plug. We  
40 characterise the relationships between key topological parameters and between connected  
41 porosity and permeability to facilitate future modelling of this process. Micro-tomographic  
42 reconstructions of a breadcrust bomb rind indicate that a deeper region with large pores, large  
43 throats, high pore volume and throat area variance and high tortuosity exists below low-  
44 permeability plugs, and this could represent a likely area for explosion-driving overpressure to  
45 develop following plug densification. A comparison of our porous micro-structure data with  
46 existing crystal micro-textures and glass volatile data from the same samples suggests that the

47 average magma ascent and decompression rates ultimately control the efficiency of magma  
48 densification, the final plug permeability and the extent of degassing of the melt phase.

49

## 50 **Keywords**

51 Plug, Porosity, Permeability, Micro-tomography, Densification, Vulcanian explosion

52

## 53 **1. Introduction**

54

55 Sequences of repeated, or cyclical, vulcanian explosions represent a frequent expression of  
56 andesitic-dacitic volcanism at arc volcanoes worldwide (e.g. Clarke et al., 2007; Hammer et  
57 al., 1999; Lavallée et al., 2012; Stix et al., 1997; Voight, 1999; Wright et al., 2007). These  
58 spontaneous explosions result from the emplacement of high-crystallinity, low-permeability  
59 plugs of degassed magma in the shallow conduit (<500 m, Fig. 1) (Bain et al., 2019; Clarke et  
60 al., 2007; Giachetti et al., 2010; Hammer et al., 1999; Sparks, 1997; Stix et al., 1997; Voight,  
61 1999; Wright et al., 2007). Further degassing beneath these low-permeability plugs triggers  
62 explosions when the strain rate exerted by overpressure in gas bubbles overcomes the structural  
63 relaxation rate of the magma (Clarke, 2013; Clarke et al., 2007; Coats et al., 2018; Dingwell,  
64 1996; Lavallée et al., 2012; Sparks, 1997; Stix et al., 1993). The formation of such degassed,  
65 low-permeability plugs is intimately linked to the processes of melt degassing, crystallisation  
66 and magma outgassing during magma ascent (Bain et al., 2019; Cashman and Blundy, 2000;  
67 Hammer et al., 2000, 1999; Lavallée et al., 2012; Preece et al., 2016). Tracking the evolution  
68 of porosity and permeability in ascending magmas is therefore fundamentally important for  
69 building understanding of eruption dynamics, improving ascent models and successful eruption  
70 forecasting.

71 Whereas the development of porosity, via magma vesiculation and strain, and the attainment  
72 of the percolation threshold (the threshold porosity at which magma ceases to be impermeable  
73 to gas) control the timing of permeability development, gas permeability itself controls the rate  
74 of gas loss and determines eruption style through the development or dissipation of pore  
75 pressure (Burgisser et al., 2017; Eichelberger et al., 1986; Okumura et al., 2009). As gas  
76 permeability is known to strongly depend on the topology of the porous network (Burgisser et  
77 al., 2017; Colombier et al., 2017; Degruyter et al., 2010; Gonnermann et al., 2017; Mueller et  
78 al., 2005; Saar and Manga, 1999; Wadsworth et al., 2017; Wright et al., 2009, 2006; Yokoyama  
79 and Takeuchi, 2009), the micro-structural properties of densifying magma subjected to shear  
80 and compaction hold key information regarding the timing and distribution of permeability  
81 reduction in densifying magma plugs. The spatial distribution of these properties determines  
82 whether gas escapes and pore pressures are reduced, or local pressurisation and fragmentation  
83 occurs at small-scales, possibly resulting in the formation of tuffisite veins (e.g. Kendrick et  
84 al., 2016) and the occurrence of ash venting (Cassidy et al., 2018, and references therein), or  
85 whether larger portions of the plug (and possibly lava dome) are expelled in a vulcanian  
86 explosion resulting from the development of large-scale pore overpressure (e.g. Lavallée et al.,  
87 2012; Sato et al., 1992).

88 This study aims to track the reduction of porosity and permeability during andesitic magma  
89 densification and plug formation in a well-constrained natural system and link these  
90 macroscopic properties with the micro-scale topological evolution of the porous network. In  
91 this work, we measure the porosity and permeability of andesitic ballistic bombs produced by  
92 vulcanian explosions of the 2004-2010 eruptive period of Galeras volcano, Colombia, and  
93 analyse the topology of the porous network in the pyroclasts using X-ray micro-tomography.  
94 These ballistics sample portions of the degassed ( $<0.4$  wt%  $H_2O$ ), densified magma plugs  
95 emplaced at shallow levels ( $<500$  m) prior to vulcanian explosions (Fig. 1) (Bain et al., 2019)

96 and therefore provide snapshots of the porosity, permeability and micro-structure of high-  
97 crystallinity andesitic magma at various stages of densification. We characterise the porosity-  
98 permeability relationship preserved in this sample suite and present detailed characteristics of  
99 the geometry of the collapsing porous network in order to track the micro-structural evolution  
100 of densifying andesitic plugs. We also analyse the pore structure of a sample of partially-  
101 annealed tuffisite vein material preserved in a dense ballistic bomb in order to compare the  
102 characteristics of the host andesitic plug and the material filling tuffisite veins, which are  
103 increasingly inferred to represent high-permeability pathways for gas transfer (Berlo et al.,  
104 2013; Castro et al., 2012; Kendrick et al., 2016; Kolzenburg et al., 2012). Finally, we compare  
105 this dataset with previously published crystal micro-texture and groundmass glass data from  
106 the same samples (Bain et al., 2019) and propose a conceptual model of plug formation linking  
107 magma decompression and densification rates.

108

## 109 **2. Background**

110

111 Much work has focussed on the onset and evolution of permeability and the controls on the  
112 percolation threshold during magma vesiculation (Burgisser et al., 2017; Colombier et al., 2017;  
113 Degruyter et al., 2010; Gonnermann et al., 2017; Klug and Cashman, 1996; Lindoo et al., 2017;  
114 Rust and Cashman, 2004; Saar and Manga, 1999; Takeuchi et al., 2005; Wright et al., 2006,  
115 2009). Changes in porosity and permeability during densification have been studied in crystal-  
116 poor magma (Ashwell and Kendrick et al., 2015; Gonnermann et al., 2017; Kennedy et al.,  
117 2016) and initially granular volcanic materials, e.g. welding ignimbrites (Heap et al., 2015;  
118 Wright and Cashman, 2014) and sintering crystal-free (Wadsworth et al., 2016) and crystal-  
119 rich (Kendrick et al., 2016) droplets. However, comparatively less is known regarding the

120 evolution of porosity and permeability during the densification of high-crystallinity magma, a  
121 process that is key to understanding the formation of low-permeability plugs, effusive-  
122 explosive transitions and the timing and magnitude of vulcanian explosions. Recent studies  
123 examining the process of magma densification under isotropic stress have shown that  
124 permeability is only slightly reduced by surface tension over relatively long periods of time,  
125 and the densification process is further lengthened by the presence of crystals (Kennedy et al.,  
126 2016; Okumura et al., 2013). Similarly the presence of crystals in initially granular densifying  
127 materials delays the sintering process, which can influence the development of pressurisation  
128 and gas-and-ash explosion cycles (Kendrick et al., 2016). Further studies involving the high-  
129 temperature (anisotropic) compression of near-aphyric pumice showed more efficient closure  
130 of void space and a corresponding decrease in permeability and increase in permeability  
131 anisotropy (parallel and perpendicular to shear), but the application of shear stress failed to  
132 completely close the pore space in even relatively crystal-poor magmas, which compacted to a  
133 threshold porosity (Ashwell and Kendrick et al., 2015). Experimental work on high-  
134 crystallinity andesites has shown that magma rheology evolves variably during shear, as at high  
135 strain rates shear may trigger dilation and creation of pore space via tearing and fracturing  
136 (Lavallée et al., 2013) or compaction of the porous network, via pore flattening and closure  
137 (Heap et al., 2017; Kendrick et al., 2013). Thus, both the degree of densification and the  
138 timescale over which it occurs may be intrinsically linked to the stress field, and hence the  
139 depth at which a magma plug forms.

140 Many studies have suggested the existence of a hysteresis in the porosity-permeability  
141 relationship in magma (e.g. Saar & Manga 1999; Rust & Cashman 2004; Wright et al. 2009;  
142 Michaut et al. 2009; Gonnermann et al. 2017). Permeability development during vesiculation  
143 is thought to occur once a system-spanning permeable pathway develops at the onset of the  
144 percolation threshold. The percolation threshold itself may depend on many factors, such as

145 composition, crystallinity and strain history. During densification, higher permeability may be  
146 maintained to low values of porosity by retaining bubble interconnections that may not exist at  
147 a similar porosity during vesiculation, due to the nature of densification (Kennedy et al., 2016),  
148 the presence of micro-fractures (Kushnir et al., 2017; Mueller et al., 2005), and the presence of  
149 crystals that hinder the closure of pores (Ashwell and Kendrick et al., 2015; Kennedy et al.,  
150 2016) and enhance the opportunity for bubble interconnections (Laumonier et al., 2011; Lindoo  
151 et al., 2017). As a result, porosity-permeability evolution paths during vesiculation and  
152 densification may differ significantly (Ashwell and Kendrick et al., 2015; Colombier et al.,  
153 2017; Gonnermann et al., 2017; Rust and Cashman, 2004; Saar and Manga, 1999; Wright et  
154 al., 2009). Michaut et al. (2009) showed that taking account of hysteretic permeability in  
155 magma ascent models could generate low-permeability plugs over a short distance, illustrating  
156 the importance of constraining the micro-structural processes that control permeability  
157 reduction in densifying magma to improve existing ascent models.

158

### 159 **3. Materials & Methods**

160

#### 161 3.1 Sample selection

162

163 For permeability and porosity measurements, nineteen andesitic ballistic bombs from the 2004-  
164 2010 period of activity of Galeras volcano were collected from the caldera rim with the  
165 assistance of the Geological Survey of Colombia (Servicio Geológico Colombiano, SGC). The  
166 stratified nature of magma plugs at Galeras volcano gave rise to three types of ballistic bombs  
167 as a result of the competition between syn-eruptive quenching and interior vesiculation of the  
168 pyroclast (Fig. 1), as described in Bain et al. (2019). The water content of the melt phase in  
169 magma that produced dense and scoriaceous bombs was too low (<0.4 wt% H<sub>2</sub>O; Bain et al.,

170 2019) to result in vesiculation on eruptive timescales (Hoblitt and Harmon, 1993; Wright et al.,  
171 2007) due to the speciation of water in rhyolitic melt at very low water contents, comprising  
172 primarily hydroxyl groups rather than molecular water available to partition into the vapour  
173 phase (Silver et al., 1990). Hence, dense and scoriaceous bombs are considered to adequately  
174 preserve pre-eruptive magma textural properties such as vesicle size and shape, as well as  
175 porosity and permeability, with the caveat that overprinting modifications to the porous  
176 network may have been sustained due to strain during bomb flight and impact. Inflated bombs  
177 typically have a bread-crust morphology due to higher melt water contents ( $>0.4$  wt%  $H_2O$ ;  
178 Bain et al., 2019) that allowed them to partially vesiculate on eruptive timescales, resulting in  
179 a pumiceous interior due to vesiculation and a dense rind due to quenching and a syn-eruption  
180 bubble nucleation delay (Wright et al., 2007). Hence, in the case of inflated bombs, only the  
181 dense rind adequately preserves the pre-eruptive magma properties. In this study, we focus on  
182 the dense and scoriaceous bombs that did not vesiculate upon explosive decompression as we  
183 probe the pre-eruptive properties of the most degassed part of the plugs. These bombs can be  
184 identified in the field by their dense appearance and lack of bread-crust morphology (Fig. 1).

185 Among the dense and scoriaceous bombs selected, ballistics covering the full range of  
186 porosities observed in the field were collected so as to give the most detailed representation of  
187 samples through the average andesitic plug at Galeras volcano. Connected porosity and  
188 permeability measurements were performed on these nineteen samples. Eight of these samples  
189 covering the range of measured porosities were then selected for X-Ray micro-tomography to  
190 investigate the topology of the porous network. Micro-tomography data were also collected for  
191 nine additional dense and scoriaceous samples from the study of Bain et al. (2019), six of which  
192 have known eruption dates, quantified feldspar micro-textures and glass volatile analyses. One  
193 sample from the dense rind of a breadcrust (inflated) bomb was also found to be suitable for  
194 micro-tomography, as it was un-fractured and thick enough to provide a sufficient volume.

195 Finally, a sample of tuffisite material from a vein hosted in a dense bomb was also imaged by  
196 micro-tomography to compare the nature of the porous network in tuffisites and the host  
197 andesite (comprising dense bombs, scoriaceous bombs and the breadcrust bomb rind). Table 1  
198 lists the samples used in this study and the analyses performed.

199

### 200 3.2 Porosity and permeability measurements

201

202 All porosity and permeability measurements were conducted in the Experimental  
203 Volcanology and Geothermal Research Laboratory at the University of Liverpool. 26 mm-  
204 diameter cores were produced from the selected bomb samples. Most samples appeared  
205 isotropic but cores were cut perpendicular to the direction of vesicle elongation in two  
206 samples where this was visually discernible (GAL9 & GAL16). The ends of each core were  
207 then ground parallel to lengths ranging 40.66-54.33 mm. Cores were washed in an ultrasonic  
208 bath and oven-dried overnight at 70 °C. The fraction of connected pores (connected porosity),  
209  $\phi_c$ , of each core was quantified by gas displacement pycnometry using an AccuPyc 1340  
210 helium pycnometer developed by Micromeritics. This instrument measures the skeletal  
211 volume of the sample (i.e. the fraction of rock and isolated pores),  $V_s$ , with an accuracy of  
212  $\pm 0.1$  %. Together, this volume and the geometrical volume of a core specimen,  $V_c$ , may be  
213 used to compute the fraction of connected pores via:  $\phi_c = (V_c - V_s)/V_c$ . The propagated  
214 uncertainty on our measurements of connected porosity is  $\pm 0.8$  %, taking into account the  
215 error on the sample measurements (assumed to be  $\pm 0.01$  mm) and the error on the measured  
216 skeletal volume.

217 Darcian (laminar) permeability,  $k$ , at confining pressures of 0.7, 1.4 and 2.1 MPa was  
218 determined for each sample using a steady-state nitrogen gas permeameter (GasPerm)

219 developed by Vinci technologies and the constant flow-rate method. For this set-up, samples  
220 are placed within a chamber housing a rubber sleeve surrounded by nitrogen gas to control the  
221 confining pressure applied onto the sample. The instrument then varies the flow rate of nitrogen  
222 across the sample until the inlet pressure stabilises (with fluctuations smaller than 0.0004  
223 MPa/min). Whilst the flow rate is held steady, the inlet and outlet pressure (in this case,  
224 atmospheric conditions) are monitored, in order to calculate the permeability using Darcy's  
225 Law (Darcy, 1857, 1856). Additionally, both Forchheimer (Whitaker, 1996) and Klinkenberg  
226 coefficients (Klinkenberg 1941) are calculated to determine the maximum allowable flow rate  
227 that satisfies Darcy conditions (meaning laminar flow conditions are satisfied and no gas  
228 slippage occurs along the walls of the void space). The propagated uncertainty associated with  
229 our permeability measurements is  $\pm 3\%$ , taking into account the accuracy of the gas flow meter  
230 and the pressure transducer on the GasPerm instrument. We acknowledge that the permeability  
231 of magma and that of the solid pyroclasts that we measure, produced from the quenching of  
232 fragmented magma plugs, will not be identical. However, as it is currently technically and  
233 financially challenging to measure the permeability of high-temperature magma samples and  
234 as we are interested in the changes in permeability across the sample set, we use the  
235 permeability range of our solid ballistic bomb samples to represent the range of magma  
236 permeability within the Galeras plugs.

237

### 238 3.3 Vesicle textures

239

240 Cylindrical cores of rock 8 mm in diameter were drilled from each sample selected for micro-  
241 tomography. These cores were drilled parallel to the long axis of the larger cores used for  
242 porosity and permeability measurements for the samples where these were measured. For the  
243 inflated bomb rind sample, a core was drilled from the dense rind and this core did not include

244 any material from the vesicular bomb interior. The cores were then washed in an ultrasonic  
245 bath for a period of several minutes and were oven-dried overnight.

246 X-ray micro-tomography was carried out in the Experimental Geosciences Facility at the  
247 University of Edinburgh. Cores were scanned using a cone beam geometry and a peak X-ray  
248 energy of 120 keV. A 0.8 mm thick aluminium energy filter was positioned between the sample  
249 and the camera to reduce beam hardening effects. For each scan, 1500-2000 projections were  
250 acquired through a 360° rotation, each with an exposure time of 1 s. Tomographic slices were  
251 reconstructed from the projections using Octopus v8.9 software (Dierick et al., 2004). During  
252 reconstruction, a further beam hardening correction and a filter for ring artefacts were applied.  
253 Reconstructed slices of the scanned volume consist of tiff files of 16 bit greyscale images  
254 (examples are shown in Fig. 5). The pixel resolution of these images ranged from 7.754-10.736  
255  $\mu\text{m}$  and the "real" resolution of objects in the resulting data volume (considered to be two voxel  
256 lengths for practical purposes) ranged from 15.508-21.472  $\mu\text{m}$  (Supplementary File A).

257 The topology of the porous network was examined by following the method of Degruyter et al.  
258 (2010). The sequences of reconstructed greyscale images of each sample were first cropped  
259 using ImageJ software (Schneider et al., 2012) to produce a prismatic data volume. ImageJ was  
260 also used to examine histograms of the images' greyscale to select appropriate thresholds to  
261 bracket the void and solid phases (the solid phase here consists mainly of glass, feldspar,  
262 pyroxene and Fe-Ti oxide crystals, Bain et al., 2019). The 3DMA-Rock code of Lindquist &  
263 Venkatarangan (1999) was then used to analyse the 3-D spatial characteristics of the porous  
264 network.

265 The data volume was first segmented, meaning each voxel was classified as either solid or pore  
266 phase, using the two-pass indicator kriging algorithm implemented in the 3DMA-Rock  
267 program (Oh & Lindquist 1999; Lindquist & Venkatarangan 1999). The first pass utilises the  
268 threshold values extracted from ImageJ to assign most of the voxels to the solid or void phase.

269 The second pass utilises an indicator kriging method to assign the remaining voxels to one of  
270 the phases, based on the spatial covariance of the image and a minimum variance estimation  
271 (Oh & Lindquist 1999). The process of segmentation produces a new binary data volume in  
272 which voxels belonging to the void phase can be studied as a numerical porous network  
273 (Degruyter et al., 2010). It is challenging to estimate the uncertainty in our segmentation in the  
274 absence of a reference sample with known properties. We therefore estimated an error of  $\pm 2.2$   
275 % on the total volume of our segmented pore space, based on the volume difference after  
276 applying opening and closing operations to the segmented pore volume for one sample (AB23).  
277 These operations smooth out the effects of the misclassification of voxels and provide a  
278 reasonable estimate of the magnitude of the error as most of the uncertainty originates from the  
279 misclassification of the small-scale features modified by opening and closing operations.

280 Once segmented, isolated pores smaller than 10 voxels and all isolated grain phase voxels were  
281 removed in a cleaning procedure, to provide a lower limit for the resolution of the disconnected  
282 voids (equivalent to  $10^{-6}$ - $10^{-5}$  mm<sup>3</sup>, Supplementary File A) and to remove artificial isolated  
283 grains in the data volume, respectively. The medial axis, or skeleton, of the connected pore  
284 structure of each sample was then obtained. The skeleton is a simplified representation of the  
285 topology of the porous network and preserves its key geometric characteristics whilst  
286 facilitating its analysis. The skeletonisation process uses an erosion method to remove pore  
287 space voxels layer by layer from the exterior of the connected pore space object until a chain  
288 of single, connected voxels remains (Lee et al., 1994). The skeleton can then be used as a  
289 reference structure to identify specific sites in the porous network, such as branching points  
290 (nodes) or pore apertures (throats). Nodal pores correspond to vertices on the medial axis where  
291 several pore pathways meet. The 3DMA-Rock package employs a vertex merging algorithm  
292 ensuring that a nodal pore is identified as such despite the fact that it may have more than one

293 vertex lying within it. Once merged, these nodal pores have a coordination number  
294 corresponding to the number of connecting pores, which is a property of interest.

295 Where possible (i.e. where connecting paths existed) the geometric tortuosity of the porous  
296 network was estimated in 3DMA-Rock by calculating the shortest paths from influx to outflux  
297 along the three dimensions of the data volume (x, y and z directions, where the z direction  
298 corresponds to the long axis of cores used for connected porosity and permeability  
299 measurements). The tortuosity for each direction is calculated as the median of the geometric  
300 tortuosity along each possible connecting path. Pore throats were identified by creating a  
301 distance map from the medial axis to the closest grain surface. Pore throats consist of the area  
302 within the minimum closed loop linking contact points between each pore pathway edge (the  
303 contact between the void and solid phases) and a cylinder that is progressively expanded by  
304 dilation from the skeleton, on each segment of the medial axis linking nodal pores. The pore  
305 throat surface area is the minimum surface area defined by this closed loop (Fig. 2). The  
306 resulting pore network model consists of pores with associated volumes and coordination  
307 numbers, separated by pore throat surfaces with associated areas. Effective throat and pore  
308 radii were also calculated as the equivalent circular and equivalent spherical radii, respectively.

309

## 310 **4. Results**

311

### 312 4.1 Porosity and permeability of bomb samples

313

314 The permeability of the variably porous samples was measured at different confining pressures  
315 (Fig. 3, Table 1, Supplementary File B) within the range of magma storage pressures calculated  
316 for dense and scoriaceous bombs in the study of Bain et al. (2019). Darcy conditions were

317 achieved while measuring the permeability of all samples but GAL10, for which the  
318 Klinkenberg-corrected permeability was used to account for gas slippage along pore walls  
319 (Klinkenberg 1941), following the method described by Heap et al. (2018). We find that at a  
320 given confining pressure, measured permeability,  $k$ , is typically higher for samples with higher  
321 connected porosities,  $\phi_c$  (Fig. 3, Table 1). For each sample, measured permeability decreases  
322 with increasing confining pressure (Fig. 3). Samples with lower connected porosity ( $\phi_c \lesssim 10\%$ )  
323 and permeability tend to show a greater dependence of the permeability on confining pressure.  
324 Overall, permeability varies over five orders of magnitude ( $1.13 \times 10^{-16} - 1.63 \times 10^{-12} \text{ m}^2$  over  
325 the range of applied confining pressures) and connected porosity varies from 1.9-26.3 % (Fig.  
326 3), consistent with qualitative observations from thin sections (Fig. 4).

327 Despite the overall trend of higher permeability corresponding to samples with higher  
328 connected porosity, we note important distinctions in the permeability of certain samples with  
329 similar porosities. At a given confining pressure, samples GAL6, GAL8, GAL13 and GAL19  
330 (boxes in Fig. 3) have notably higher permeabilities (up to two orders of magnitude) than  
331 samples GAL2, GAL4, GAL9, GAL12, GAL16 with similar connected porosities (Table 1).  
332 This set of comparatively “higher-permeability” samples also shows a notably smaller  
333 dependence on confining pressure than samples with lower permeability and similar  $\phi_c$ , as well  
334 as samples with lower  $\phi_c$  (Fig. 3, Supplementary File B). Eight samples covering the full range  
335 of  $\phi_c$  were selected for further exploration by micro-tomography (Table 1), including two  
336 low/high permeability pairs with similar connected porosities (GAL4/GAL6 & GAL16/GAL8)  
337 in order to investigate any topological controls on the observed permeability difference.

338

#### 339 4.2 Quantification of vesicle textures

340

341 Samples with higher connected porosity correspond to samples with a higher areal void fraction  
342 when observed in thin section (Fig. 4). Vesicles are typically polylobate and/or branching in  
343 shape (Fig. 4), as previously described by Bain et al. (2019). Examples of reconstructed  
344 tomographic slices through the scanned cores are shown in Fig. 5 and illustrate the  
345 fundamentally different nature of the porous network in the host andesite (comprising dense  
346 bombs, scoriaceous bombs and the breadcrust bomb rind; Fig. 5a–c), which consists of  
347 interconnected, branching vesicles, and in the sample of tuffisite material (Fig. 5d), which  
348 consists of voids between partially sintered granular material. Fig. 6 shows examples of the  
349 rendered pore space and the corresponding pore network models in host andesite samples and  
350 the tuffisite sample.

351 Analysed micro-tomography data volumes ranged from 274–473 mm<sup>3</sup>. Among the samples for  
352 which connected porosity was measured, numerical porosities computed from the micro-  
353 tomography data, which represent the total porosity for a sample, ranged from 0.2–25.9%. The  
354 numerical porosities obtained are generally in good agreement with the range in measured  
355 connected porosities (Fig. 7). Numerical porosity typically underestimates the measured  
356 connected porosity by up to 5% due to the resolution limit of the micro-tomography (see section  
357 3.3). However, as this difference is small, non-systematic and relatively consistent, numerical  
358 porosity values are considered to provide an adequate measure of sample porosity for the  
359 purposes of investigating changes in the topology of the void space, and we use this as a metric  
360 to track the extent of densification.

361 Although the distributions of pore volumes, throat surface areas and pore coordination numbers  
362 computed for each sample are non-normal (Supplementary File C), we use the arithmetic mean  
363 of these distributions as an average value for each parameter that is a skewed representation of  
364 the central tendency taking into account the distribution tails (e.g. outlying larger pores and  
365 larger throats that are progressively closed as a result of densification). Median values for these

366 distributions do not vary significantly from the means (Supplementary File C) but do not  
367 capture the tails, which are expected to be important in understanding the densification process.  
368 Although there is some scatter in our data (Fig. 8), we describe the general trends here through  
369 best-fitting relationships (on the basis of the lowest root mean square error, RMSE) and discuss  
370 the possible causes of scatter in section 5.1. The RMSE for each best-fit relationship is given  
371 in Fig. 8 and the equations and RMSEs for all attempted fits are given in Supplementary File  
372 A.

373 Among the samples of host andesite, the mean pore volume and mean throat area show power  
374 law relationships with numerical porosity (Fig. 8a–b), and samples with lower numerical  
375 porosity tend to have lower mean pore volumes and mean throat areas. The rate of decrease in  
376 the mean pore volume and mean throat area with decreasing numerical porosity is relatively  
377 low above a porosity of around 10 %, and higher below this porosity (Fig. 8a–b). The  
378 volumetric number densities of connected pores (Fig. 8c) and of connected throats (Fig. 8d)  
379 each show an exponential relationship with numerical porosity, with lower porosities  
380 corresponding to lower number densities of pores and throats. The mean pore coordination  
381 number shows a power law relationship with numerical porosity (Fig. 8e). As for the mean  
382 pore volume and throat area, the rate of decrease of the mean coordination number with  
383 porosity is low above a porosity of around 10 % and higher below this porosity. The mean  
384 coordination number drops below 1 at a threshold porosity of around 0.5 % (Fig. 8e), meaning  
385 pores are typically isolated below this porosity. The volumetric number density of disconnected  
386 voids (defined as the average number of disconnected voids per  $\text{mm}^3$  of analysed material) also  
387 displays a poorly-defined power law relationship with numerical porosity, with a large amount  
388 of scatter in the porosity range 5–15% (Fig. 8f). The variance in connected pore volumes and  
389 throat areas is also higher in samples with higher numerical porosity (Fig. 8g–h). There is a  
390 strong positive relationship between the mean effective pore and mean effective throat radii

391 (Fig. 9). Tortuosity is slightly higher ( $>2.5$ ) in samples with a mean pore volume above  $0.06$   
392  $\text{mm}^3$  (Fig. 10a) and is similar ( $2\text{--}2.5$ ) for lower pore volumes. The lowest tortuosity observed  
393 in each sample decreases slightly with mean pore throat area (Fig. 10b) except for sample  
394 GAL8, and the range of tortuosity ( $2\text{--}2.6$ ) is similar for pore throat areas in the range  $1.1\text{--}1.7$   
395  $\times 10^4 \mu\text{m}^3$ . Tortuosity shows no clear relationship with the mean coordination number in each  
396 sample (Fig. 10c). The sample with the highest tortuosity and the highest anisotropy with  
397 respect to paths tortuosity in the x, y and z directions is the rind of the breadcrust bomb sample.  
398 Among samples for which connected porosity and permeability were measured (Table 1), the  
399 volumetric number density of pores, throats and disconnected voids, and the ratio of the number  
400 of throats to the number of pores (normalised by the analysed volume), are typically higher in  
401 samples with higher measured connected porosity and permeability (Fig. 11). The mean  
402 coordination number of each pore, the mean pore volume and mean throat surface area are also  
403 typically higher in samples with higher measured porosity and permeability (Fig. 11).  
404 Tortuosity is slightly higher in samples with higher measured porosity and permeability,  
405 although GAL16 shows a higher tortuosity than the other samples and GAL8 shows notably  
406 higher tortuosity in the y direction, resulting in some scatter. All micro-tomography analysis  
407 results are provided in Supplementary File A.

408 The sample taken from a tuffisite vein hosted in a dense bomb (AB2<sub>T</sub>) is characterised by much  
409 higher volumetric number densities of connected pores and throats (Fig. 8c–d). The mean pore  
410 volume and throat area in the tuffisite are also lower than in the host andesite for a similar  
411 porosity (Fig. 8a–b). The variance in pore volumes and the variance in throat areas are also  
412 very low in this sample (Fig. 8g–h). The mean pore coordination number in the tuffisite is on  
413 the higher end of the dataset and this material also features a high number density of  
414 disconnected voids (Fig. 8e–f). Tortuosity is among the lowest in the dataset for this sample  
415 (Fig. 10). The relationship between the effective throat to pore radii in this material fits with

416 the overall trend of the host andesite data (Fig. 9), but both these effective radii are on the  
417 smaller end of the dataset as a whole.

418

#### 419 4.3 Low/high permeability pairs of samples with similar connected porosity

420

421 Two pairs of samples, GAL4/GAL6 and GAL16/GAL8, with similar measured connected  
422 porosities ( $\Delta\phi_c < 1\%$ ) but permeabilities varying by two orders of magnitude (Table 2) were  
423 selected for micro-tomography in order to investigate any topological controls on the observed  
424 permeability difference. In both pairs the mean coordination number and volumetric number  
425 density of disconnected (isolated) voids are similar (Table 2).

426 In the case of pair GAL4/GAL6, the higher permeability sample (GAL6) shows a higher  
427 volumetric number density of pores and throats than the low permeability sample, and higher  
428 mean effective pore and mean effective throat radii (Table 2). The higher permeability sample  
429 also displays a lower variance in pore volumes and throat areas (Table 2). Tortuosity could not  
430 be established for the low permeability sample as there were no volume-spanning connected  
431 paths in the x, y and z directions and therefore tortuosity could not be compared for this pair of  
432 samples. In the case of pair GAL16/GAL8, the higher permeability sample (GAL8) has a lower  
433 number density of pores and throats than the low permeability sample (Table 2). Both samples  
434 exhibit a similar mean throat area and a similar variance in throat areas but the higher  
435 permeability sample has a slightly lower mean pore volume and lower variance in pore volumes  
436 (Table 2). Geometric tortuosity is higher in the low permeability sample in the x and z  
437 directions (with z representing the direction in which permeability was measured), and higher  
438 in the high permeability sample in the y direction (Table 2).

439

## 440 5. Discussion

441

### 442 5.1 Topology of the porous network

443

444 The combination of micro-tomography data and porosity and permeability measurements  
445 illuminates the topological changes in the porous network associated with magma densification  
446 in the Galeras plugs. We observe that magma densification (total porosity covering the range  
447 25.9–0.1 %) is accompanied by the progressive reduction of mean pore volume ( $7.84 \times 10^{-2} -$   
448  $2.98 \times 10^{-4} \text{ mm}^3$ ), mean throat surface area ( $2.47 \times 10^4 - 1.1 \times 10^3 \text{ } \mu\text{m}^2$ ) and mean pore  
449 coordination number (4.37–0.42) as connected porosity (26.3–1.9 %) and permeability ( $1.63$   
450  $\times 10^{-12} - 1.13 \times 10^{-16} \text{ m}^2$ ) decline. The variance in pore volumes and throat areas is also  
451 reduced ( $4.12 \times 10^{-2} - 3.89 \times 10^{-6} \text{ mm}^6$  and  $8.31 \times 10^9 - 1.91 \times 10^6 \text{ } \mu\text{m}^4$ , respectively),  
452 implying that the range of length-scales of the structures performing gas transfer at the sample-  
453 scale (pores and throats) becomes smaller. The porous medium therefore becomes more  
454 homogeneous during densification as the range of pore volumes and throat sizes decreases. The  
455 volumetric number density of connected pores ( $2.69 \times 10^1 - 1.69 \times 10^{-1} \text{ mm}^{-3}$ ) and throats  
456 ( $6.90 \times 10^1 - 2.58 \times 10^{-1} \text{ mm}^{-3}$ ) and the volume-normalised ratio of throats to pores (3.17–0.22)  
457 also decline as a result of densification.

458 Interestingly, the number density of disconnected voids is also generally reduced (94.27–1.43  
459  $\text{mm}^{-3}$ ) despite a large amount of scatter in the data (Fig. 8f & Fig. 11), suggesting that the  
460 closure and/or coalescence of isolated pores with the connected porous network typically  
461 proceeds more efficiently than the creation of new isolated pores by throat closure. We  
462 speculate that the scatter in the disconnected voids dataset, as well as in other micro-  
463 tomography datasets, could attest to differences in the amount of strain, nature of strain, or the  
464 strain rate experienced by different parcels of magma in the conduit, as high strain rates closer

465 to the conduit margins are likely to promote bubble coalescence (Okumura et al., 2009). The  
466 scatter in the mean pore volume and mean throat area datasets may also be related to syn-  
467 eruptive deformation of the porous network during magma fragmentation, bomb flight and  
468 impact.

469 The decrease in tortuosity (3.57–2.11, considered as the average tortuosity in the x, y and z  
470 directions) as mean pore volume and mean throat area are reduced shows that more direct gas  
471 transfer pathways are created as a result of densification, implying that permeability is  
472 maintained during densification until very low porosities, as observed in the permeability  
473 measurements and in previous studies (Ashwell and Kendrick et al., 2015; Gonnermann et al.,  
474 2017; Heap et al., 2015; Kendrick et al., 2013; Kennedy et al., 2016; Okumura and Sasaki,  
475 2014). As the number densities of pores and throats typically decline during this process,  
476 implying that bubbles and bubble connections are progressively lost (Fig. 8c–d & Fig. 11), we  
477 suggest that these more direct pathways result from the rearrangement of pores and throats, as  
478 well as bubble coalescence, during viscous deformation of the magma plug and, thus, of the  
479 porous network. We also note that the number density of connected pores appears to decline at  
480 a lower rate as a result of densification than the number density of throats until very low  
481 porosities (2–3%) are attained (Fig. 8c–d), suggesting the importance of the concerted  
482 processes of throat closure, formation of disconnected voids, and connection of disconnected  
483 voids to the connected porous network.

484 Micro-tomography data from the sample taken from a tuffisite vein preserved in a dense bomb  
485 show that the average pore volume and pore throat surface area are much smaller in the tuffisite  
486 material than in the host andesite (Fig. 8a–b), confirming qualitative observations from the  
487 reconstructed tomographic slices (Fig. 5). The number densities of pores and throats are much  
488 higher in the tuffisite (Fig. 8c–d), the mean coordination number is among the highest in the  
489 dataset (Fig. 8e) and the tortuosity is among the lowest in the dataset (Fig. 10). The number

490 density of disconnected voids is comparatively high, and the variance in pore volume and in  
491 throat area are both very low (Fig. 8f–h). These data show that the porous network in the  
492 tuffisite vein material is characterised by small, well-connected pores and throats with narrow  
493 size-distributions, between ash-size fragments of andesite. Despite the small throat sizes, this  
494 material features more direct pathways for gas transfer due to the low tortuosity, which may  
495 constitute the primary reason that tuffisites represent high-permeability pathways despite the  
496 small scale of the micro-structures performing gas transfer (Berlo et al., 2013; Castro et al.,  
497 2012; Kendrick et al., 2016; Kolzenburg et al., 2012; Tuffen et al., 2003).

498

## 499 5.2 Porosity, permeability and micro-structural changes resulting from the densification of 500 high-crystallinity andesitic magma

501

### 502 *Quantification of key relationships*

503

504 Compiled porosity-permeability datasets from previous studies of various types of volcanic  
505 pyroclasts highlight a large amount of scatter that is thought to originate from different  
506 decompression rates and degassing, outgassing and deformation processes affecting magma  
507 erupted effusively and explosively (e.g. Rust & Cashman 2004; Mueller et al. 2005). Previous  
508 authors have provided general relationships between total porosity and permeability for  
509 volcanic products that are in the form of power laws based in percolation theory and are  
510 constrained empirically (Blower, 2001; Costa, 2006; Klug and Cashman, 1996; Mueller et al.,  
511 2005; Saar and Manga, 1999). The topology of the porous network exerts a primary influence  
512 on the porosity-permeability relationship (e.g. Bear 1972; Rink 1976; Doyen 1988), for  
513 example the geometry and connectivity of pores in compacting granular systems may contrast

514 markedly with the micro-structures arising from vesiculation in lavas and pyroclasts  
515 (Colombier et al., 2017; Heap et al., 2015; Klug and Cashman, 1996; Mueller et al., 2005;  
516 Okumura and Sasaki, 2014; Saar and Manga, 1999; Wadsworth et al., 2016; Wright et al., 2009,  
517 2006; Yokoyama and Takeuchi, 2009), as observed in the previous section. In particular, pore  
518 sizes, pore throat sizes and tortuosity are expected to exert a large influence on permeability  
519 (Degruyter et al., 2010; Saar and Manga, 1999; Zhu and Wong, 1996), as is the extent and  
520 anisotropy of heterogeneity (e.g. the variance of the size distributions of pores and throats)  
521 (Bernabé et al., 2003; Bernabé and Bruderer, 1998; Farquharson et al., 2016) and the presence  
522 of fractures (Heap and Kennedy, 2016; Lamur et al., 2017; Lavallée et al., 2013) whose  
523 longevity may vary with healing timescales (Lamur et al., 2019).

524 As the topology of the porous network in Galeras samples originates from the specific  
525 degassing and deformation processes operating during the densification of high-crystallinity  
526 andesitic magma, a primary motivation of this study is to establish quantitative relationships  
527 that may be used in the future modelling of this process. We fit simple power law regressions  
528 by non-linear least squares fitting to our micro-structural datasets in order to characterise these  
529 relationships in the well-constrained Galeras system (Fig. 12a–c). We excluded data for the  
530 sample of tuffisite material from the fitting procedure as we are primarily interested in the  
531 micro-structural changes of the porous network in the host andesite during densification of  
532 coherent magma, rather than sintering of granular material. We find that the mean throat area  
533  $t_a$  varies with the mean pore volume  $p_v$  as:  $t_a = 1.058 \times 10^5 p_v^{0.6}$  (RMSE: 3345  $\mu\text{m}^2$ ). The  
534 volumetric number density of throats  $t_n$  varies with the number density of pores  $p_n$  as:  $t_n =$   
535  $2.082 p_n^{1.331}$  (RMSE: 0.63  $\text{mm}^{-3}$ ), where we excluded one very dense sample (AB37, shown  
536 in black in Fig. 12b) from the fitting procedure as the mean coordination number is 0.4,  
537 indicating that the average pore is not connected to any other pores, and this may explain why  
538 it forms a clear outlier in the dataset. The mean throat effective radius  $t_{eff}$  varies with the mean

539 effective pore radius  $p_{eff}$  as:  $t_{eff} = 0.9126 p_{eff}^{0.81}$  (RMSE: 5.3  $\mu\text{m}$ ). For this relationship, one  
540 very dense sample (GAL5) was excluded from the fitting procedure as the analysis of the  
541 micro-tomography data resulted in one pore and no throats after the data cleaning steps. This  
542 sample forms a clear outlier in Fig. 10c.

543 In order to provide a quantitative relationship between connected porosity  $\phi_c$  and permeability  
544  $k$  for future modelling of the densification process, we attempted to fit our data using a power  
545 law relationship ( $k = 5.56 \times 10^{-17} \phi_c^{2.96}$ , RMSE:  $4.02 \times 10^{-13} \text{ m}^2$ ; shown in Fig. 13).  
546 However, we found that the power law relationship did not provide a satisfactory fit to the  
547 Galeras data over the 0–15 % range of connected porosity (Fig. 13). Despite a slightly higher  
548 error, we find that an exponential relationship provides a more satisfactory fit, especially over  
549 the 0–15 % range of connected porosity:  $k = 5.46 \times 10^{-17} e^{0.38\phi_c}$  (RMSE:  $4.52 \times 10^{-13} \text{ m}^2$ ).  
550 For example, for a connected porosity of 7 %, the best-fit power law relationship overestimates  
551 permeability by approximately two orders of magnitude (Fig. 13). Our micro-tomography data  
552 show that the densification of high-crystallinity porous andesites during plug formation is  
553 expressed as decreasing 1) pore volumes, 2) pore throat areas, 3) volumetric number densities  
554 of pores, throats and disconnected voids, 4) the variance of pore volumes and pore throat areas,  
555 and 5) tortuosity. The best-fit exponential porosity-permeability relationship reflects these  
556 micro-structural changes and may be generally appropriate for modelling the densification and  
557 plug formation process in high-crystallinity andesitic magmas, as this relationship is distinct  
558 from that characterising both vesiculating magmas (Klug and Cashman, 1996; Mueller et al.,  
559 2005) and densifying, sintering initially granular systems (e.g. welding ignimbrites (Heap et  
560 al., 2015; Wright and Cashman, 2014) and tuffisites (Wadsworth et al., 2016)).

561

562 *Implications*

563

564 The porosity-permeability relationship in ballistic bombs sampling Galeras magma plugs is not  
565 consistent with published porosity-permeability data or relationships formulated for explosive  
566 products (Fig. 13) (Hill, 1984; Rust and Cashman, 2004; Tait, 2004; Wright et al., 2007, 2006).  
567 In contrast, our data agree well with measurements from previous studies on high-crystallinity  
568 andesite dome lavas or blocks in block-and-ash flows from Volcán de Colima (Farquharson et  
569 al., 2015) and Mount Pelée (Bernard et al., 2007; Jouniaux et al., 2000). Our data are consistent  
570 with the notion of a porosity-permeability hysteresis in the context of densifying high-  
571 crystallinity magma plugs, as they follow the trend of evolving porosity and permeability in  
572 effusive samples thought to reflect an advanced stage of bubble interconnection and collapse  
573 (Mueller et al., 2005), rather than explosive samples reflecting various extents of vesiculation  
574 and bubble interconnection.

575 Our samples were not erupted effusively, but by examining ballistics that did not vesiculate  
576 upon eruptive decompression (Bain et al., 2019), we aim to shed light on the pre-explosive  
577 magma conditions prevailing in shallow conduit plugs at Galeras volcano, which are akin to  
578 dome lavas erupted effusively at the surface at other andesitic stratovolcanoes. Lava dome  
579 emplacement and the congruent development of a shallow conduit plug prior to vulcanian  
580 explosions may explain why dome lavas and block-and-ash flow samples follow a similar  
581 porosity-permeability trend as Galeras ballistics, as the porous micro-structures in these  
582 samples seemingly record the same conduit/dome densification processes. In contrast, other  
583 types of effusive products (with different compositions and/or different emplacement  
584 mechanisms) may record other processes that affect the porous network (Colombier et al.,  
585 2017), e.g. vesiculation or bubble shearing during flow. This generally good agreement  
586 supports the idea that the relationships extracted from our data could be used as a first order  
587 proxy in modelling the densification process during the emplacement of degassed, highly-

588 crystalline lava domes and plugs. In this context, our data suggest that the decrease in tortuosity  
589 (Fig. 10) during densification may be an important process in maintaining permeability to low  
590 porosities, permitting plug and dome emplacement and promoting a volcanic style  
591 characterised by effusive-explosive transitions.

592 High-temperature experimental compaction studies of natural crystal-poor rhyolite (Ashwell  
593 and Kendrick et al., 2015; Gonnermann et al., 2017), crystal-rich rhyolite (Ashwell and  
594 Kendrick et al., 2015) and crystal-rich andesite (Kendrick et al., 2013; Lavallée et al., 2013)  
595 lavas show contrasting porosity-permeability-strain pathways that emphasise the importance  
596 of the nature of the starting material and the strain history. Ashwell and Kendrick et al. (2015)  
597 found that crystal-rich (60-70 % of the solid fraction) rhyolite dome samples achieved a  
598 compaction limit of 17-19 % porosity, whereas crystal-poor (5% of the solid fraction) rhyolite  
599 dome samples likely had a much lower compaction limit that was not achieved in the 60 %  
600 strain limit set in their experiments. In that study, crystals hindered the reduction in porosity  
601 and permeability during unconfined compaction, whereas natural Galeras samples clearly  
602 reached much lower porosities during densification, possibly as a result of the confining  
603 pressure in the conduit/dome setting. Gonnermann et al. (2017) observed that the high-  
604 temperature, unconfined deformation of crystal-poor pumices resulted in permeability being  
605 retained to low values of porosity (<20 %), however our data do not follow the same porosity-  
606 permeability reduction pathway (Fig. 13), likely as a result of the difference in deformation  
607 conditions (unconfined experimental conditions versus confined natural compaction) and  
608 starting material (high-crystallinity andesite versus crystal-poor pumice). In unconfined  
609 experiments on high-crystallinity andesites, Kendrick et al. (2013) found that samples  
610 deformed to 20 % strain, under low applied stresses to ensure a predominantly viscous response,  
611 resulted in a small reduction in porosity and reduction in permeability by two orders of  
612 magnitude, whereas those deformed more rapidly were subject to an increase in porosity while

613 permeability remained unaffected (parallel to compaction). This suggests that confined natural  
614 compaction at low strain rates played an important role in allowing the high-crystallinity  
615 Galeras samples to densify to very low connected porosities (1.92 %).

616 The differences in pore and throat properties and tortuosity for low/high permeability pairs of  
617 samples described in section 4.3 do not satisfactorily explain the two order of magnitude  
618 difference in measured permeability at a given porosity, nor the observed reduced dependence  
619 of permeability on confining pressure. We therefore suggest that the low/high permeability  
620 pairs in the Galeras sample set may reflect various micro-fracture densities that were not  
621 detected in hand sample and were below the resolution of micro-tomography (15–21  $\mu\text{m}$ , see  
622 section 3.1), as fractures have been observed to have a dominant effect on permeability in  
623 previous studies (Berkowitz, 2002; Heap and Kennedy, 2016; Lamur et al., 2017; Lavallée et  
624 al., 2013; Matthäi and Belayneh, 2004). These fractures may have formed either during pre-  
625 eruptive deformation as in the study of Kendrick et al. (2013) or during syn-eruptive cooling  
626 (e.g. Browning et al., 2016; Lamur et al., 2018) or impact (e.g. Lavallée et al., 2013) of the  
627 Galeras bombs.

628

### 629 5.3 Tuffisite

630

631 Although a rigorous study of the porosity and permeability of tuffisite veins is beyond the scope  
632 of this paper, our micro-tomography data from the sample of tuffisite material analysed here  
633 reflects the fundamentally different structure of the porous network compared to the host  
634 andesite. In contrast to the host andesite, which exhibits a porous structure arising from the  
635 growth, coalescence and collapse of gas bubbles in high-crystallinity magma, tuffisite veins  
636 host structures arising from gas-and-ash flow through a fracture followed by settling,

637 compaction and sintering of a granular medium (Kendrick et al., 2016; Tuffen et al., 2003;  
638 Wadsworth et al., 2016). Their prevalence in Galeras ballistic samples of all types (Bain et al.,  
639 2019) suggests that, despite the retention of permeability during densification of the host  
640 andesite, the permeability of localised areas of the magma plugs became insufficient to  
641 efficiently dissipate pore pressure, resulting in local fragmentation and the formation of  
642 fractures filled with fragmental materials. However, the low tortuosity of porous pathways in  
643 this sample suggests that tuffisites represented high permeability pathways within the magma  
644 plug with a potentially important role for degassing prior to vulcanian explosions, as shown in  
645 previous studies on tuffisite veins (Berlo et al., 2013; Castro et al., 2014, 2012; Kendrick et al.,  
646 2016; Kolzenburg et al., 2012; Saubin et al., 2016). This is consistent with the study of Bain et  
647 al. (2019) on these ballistic bombs, which suggested that the flux of a S-rich gas phase through  
648 these veins served to locally deplete the interstitial melt of the host andesite with respect to  
649 H<sub>2</sub>O, F and Cl and cause S to become enriched in the melt phase.

650

#### 651 5.4 Implications for eruption dynamics

652

##### 653 *Porous micro-structure and crystal micro-textures*

654

655 Bain et al. (2019) related magma ascent and decompression rates and eruption dynamics at  
656 Galeras volcano to systematic variations in plagioclase microlite number density, characteristic  
657 size and aspect ratio. Smaller volume explosions in 2004-2008 produced ballistics with crystal  
658 micro-textures characterised by small numbers of large, prismatic microlites, whereas larger  
659 volume explosions in 2009-2010 produced ballistics with high numbers of small, tabular  
660 microlites (Bain et al., 2019). Based on a comparison of these crystal micro-textures with

661 results of decompression experiments by Brugger and Hammer (2010), these changes were  
662 determined to have been driven by increasing average decompression rates from 1–10 MPa/h  
663 due to increasing magma ascent rates (Bain et al., 2019). Increasing decompression rates  
664 resulted in increasing crystal nucleation rates and decreasing crystal growth rates over the  
665 course of the eruption sequence, and gave rise to higher plagioclase microlite number densities,  
666 smaller characteristic sizes and a change from prismatic to tabular microlites. Here, we  
667 compare the plagioclase microlite volumetric number density ( $N_v$ ), the crystal aspect ratio (S/L,  
668 corresponding to the best-fit microlite short axis/long axis) and the characteristic microlite size  
669 from the samples in the study of Bain et al. (2019) with the corresponding micro-tomography  
670 data collected here to investigate any relationships between the crystal micro-structure and the  
671 porous micro-structure (Fig. 14). We find that samples with low  $N_v$ , low S/L and large  
672 characteristic size (corresponding to crystal micro-textures with small numbers of large,  
673 prismatic microlites) typically feature porous networks with higher mean pore volumes and  
674 mean throat areas (Fig. 14a–c), as well as higher variance in pore volumes and throat areas.  
675 Conversely, samples with high  $N_v$ , high S/L and small characteristic size (corresponding to  
676 crystal micro-textures with high numbers of small, more tabular microlites) typically feature  
677 porous networks with lower mean pore volumes, lower mean throat areas (Fig. 14 a–c), as well  
678 as lower variance in pore volumes and throat areas. The breadcrust bomb rind sample features  
679 a porous network that is most similar in nature to the porous network in samples with low  $N_v$ ,  
680 low S/L and large characteristic size (Fig. 14). This suggests that andesitic plugs that develop  
681 in magma ascending and decompressed at lower average rates (resulting in low  $N_v$ , low S/L  
682 and large microlite characteristic size) are characterised by a crystal micro-texture that  
683 facilitates the retention of the porous network, perhaps as a result of inefficient densification,  
684 to produce a comparatively high-permeability plug. This is supported by the observation that  
685 the porous network in the breadcrust bomb rind, which records the porous micro-structure in

686 the deepest part of the plug prior to the onset of densification, is most similar to ballistics  
687 produced following slow magma ascent. In addition, the presence of lava domes associated  
688 with the explosions that produced these ballistic samples (Bain et al., 2019) suggests that pore  
689 pressures were effectively dissipated so that lava effusion was possible and repose times  
690 between vulcanian explosions became long (hundreds of days). Conversely, plugs that develop  
691 in magma ascending and decompressed at higher rates (resulting in high  $N_v$ , high S/L and small  
692 microlite characteristic size) host porous networks that have undergone significant  
693 densification, producing a comparatively low-permeability plug allowing overpressure to build  
694 up rapidly, consistent with the short repose times between explosions (tens of days) noted  
695 during 2009-2010 (Bain et al., 2019). We suggest that these differences could be the result of  
696 a rheological control on the efficiency of densification as a result of the variation in crystal  
697 micro-textures. We propose that large, prismatic microlites (low S/L) in these magmatic  
698 suspensions are likely to interact more frequently and produce higher bulk magma viscosities  
699 than smaller, more tabular microlites (high S/L) (Klein et al., 2018; Mueller et al., 2005), and  
700 this could explain the inferred variations in densification efficiency. These rheological  
701 variations will be further investigated in future work.

702

### 703 *Porous micro-structure and groundmass glass volatiles*

704

705 The decrease in connected porosity and permeability as pore volumes, throat areas and the  
706 number densities of pores and throats decrease shows that the change in topology of the porous  
707 network controls the ability of the densifying magma plug to permit gas flow. However, the  
708 timescale over which densification occurs, which may vary significantly due to the rheological  
709 differences inferred in the previous section, is also likely to control the ability for a magma  
710 plug to degas and outgas. Groundmass glass volatile analyses from Bain et al. (2019) are

711 available for ten of the samples for which micro-tomography data were collected (Fig. 15).  
712 These volatile data show that F and Cl follow an overall trend of depletion in the groundmass  
713 glass with reducing pore and throat sizes (Fig. 15c–d), despite the occurrence of occasional  
714 outliers (e.g. F: 860 ppm, 819ppm and 673 ppm; Cl: 2234 ppm) that may be related to the  
715 complex effects of vapour fluxing from depth through degassed magma stored at shallow levels  
716 in the conduit (e.g. Bain et al., 2019; Rust et al., 2004; Wright et al., 2007). However, H<sub>2</sub>O data  
717 reveal an opposite trend (Fig. 15a), with lower groundmass glass water contents generally  
718 corresponding to larger pore and throat sizes. In the previous section, we observed that these  
719 H<sub>2</sub>O-poor samples correspond to magma plugs that densified inefficiently, possibly as a result  
720 of rheological controls (e.g. microlite number densities, sizes and shapes) that maintain bubble  
721 inter-connections, leading to relatively high-permeability plugs. We suggest that the opposite  
722 trend in H<sub>2</sub>O and halogen data is related to a trade-off in the rate of densification with respect  
723 to the diffusion rate of each species. Rapidly densifying magma plugs (characterised by high  
724  $N_v$ , high S/L, small characteristic microlite sizes and low mean pore volumes and mean throat  
725 areas) record higher groundmass glass H<sub>2</sub>O contents due to the relatively rapid disruption of  
726 connected porous pathways and hence rapid destruction of surfaces for diffusive exchange (Fig.  
727 16b). More inefficient densification (in magma plugs characterised by low  $N_v$ , low S/L, large  
728 characteristic microlite sizes and higher mean pore volumes and mean throat areas) results in  
729 connected porous pathways remaining open and more extensive degassing of the melt phase  
730 with respect to rapidly-diffusing volatile species, such as H<sub>2</sub>O (Fig. 16a). In contrast, the slower  
731 rates of diffusion of F and Cl (Bai and Koster van Groos, 1994) result in a groundmass glass  
732 halogen signature that records magma degassing during emplacement at shallow levels and  
733 does not record an effect related to the rate of densification (Fig. 15c–d). In other words, the  
734 glass F and Cl contents record progressive degassing during magma emplacement in the  
735 shallow conduit, whereas the glass H<sub>2</sub>O content records the overprinting process of contrasting

736 densification rates in magma plugs with different crystal micro-textures and, potentially,  
737 rheology (i.e. rapid or slow disruption of porous network connections with apparent viscosity  
738 as a limiting factor) as a result of the more rapid diffusion rate. This model is supported by the  
739 groundmass glass volatile content of the breadcrust bomb rind, which is sourced from a region  
740 in the conduit below the main degassed plug that we focus on in this study. The breadcrust  
741 bomb rind contains a similar amount of CO<sub>2</sub>, F, Cl and S (Fig. 15b–e) and a similar porous-  
742 microstructure (Fig. 14) as the bombs that have undergone the least amount of densification.  
743 However, this sample contains a higher water content than all bombs sourced from the degassed  
744 region (Fig. 15a), showing that the magma underlying the plugs likely contained a relatively  
745 high water concentration before the onset of densification. We therefore propose that, of the  
746 volatiles discussed here, water is the only species that diffused rapidly enough to record the  
747 differences in plug densification rate prior to vitrification of the groundmass upon ballistic  
748 expulsion (Fig. 15-16).

749

#### 750 *Porous micro-structure beneath the degassed plug*

751

752 Most breadcrust bombs from Galeras volcano have dense rinds (0–0.5 %), showing that dense  
753 magma is stored immediately below the most degassed region of the plugs (100–500 m, Bain  
754 et al., 2019). The breadcrust bomb studied here, however, preserves an unusually vesicular rind  
755 (~17 %) giving insights into the porous network in magma stored deeper in the conduit (>500  
756 m). The sample taken from the rind of this breadcrust bomb has the largest mean pore volume  
757 and mean throat area (Fig. 14), as well as the largest pore volume and throat area variance in  
758 the sample set. The porous network in this rind is also the most tortuous and shows a significant  
759 anisotropy in tortuosity in three dimensions (Fig. 10). The magma underlying the plugs  
760 therefore comprised the highest gas fraction and contained the largest amount of dissolved

761 volatiles in the melt phase, and yet the permeability of this zone may have been limited by the  
762 highly contorted paths channelling gas escape.

763 Bain et al. (2019) inferred higher degassing-driven effective undercooling in magma below the  
764 most degassed part of the plug in order to explain consistently higher microlite  $N_v$  in deeper-  
765 sourced breadcrust bombs relative to dense and scoriaceous bombs. The large mean pore  
766 volumes, mean throat areas and high variance in the scales of the porous micro-structures in  
767 this breadcrust bomb rind support the idea of a larger degassing increment in the area below  
768 the plugs, as gas flow localisation through preferred pathways is expected to occur in highly  
769 heterogeneous porous media (Bernabé and Bruderer, 1998; Laumonier et al., 2011; Lavallée et  
770 al., 2013; Wright and Weinberg, 2009) and may have initially promoted rapid outgassing.  
771 However, the propensity for gas flow localisation may eventually be countered by the high  
772 tortuosity of the connected pathways during ongoing degassing.

773 These observations support the hypothesis from Bain et al. (2019) that the region of the magma  
774 column emplaced in the shallow conduit where significant overpressure is likely to have  
775 developed is located below the degassed, low-permeability plugs, as previously suggested in  
776 the studies of Clarke et al. (2007), Giachetti et al., (2010), Hammer et al. (1999); Sparks (1997),  
777 and Wright et al. (2007). We therefore propose the following model for vulcanian explosions  
778 as Galeras volcano. Prior to individual vulcanian explosions, pore pressures within the  
779 viscously compacting andesitic magma plug emplaced in the shallow conduit (<500 m) were  
780 decreasing, as we have shown here that permeability was largely retained within the magma  
781 plugs and densification could occur without the development of large-scale pore overpressure.  
782 We propose that only small-scale, localised pore overpressure developed within the plugs,  
783 evidenced by the occurrence of tuffisite veins. In contrast, the high variance in pore sizes and  
784 throat areas in the region below the degassed plugs, as evinced by the porous network in the  
785 breadcrust bomb rind, may have enhanced the possibility for pore overpressure development

786 by forcing rapidly moving gas to stall in pores with smaller throats or to rapidly infiltrate  
787 smaller pores through large throats during gas flux. The results of this study suggest that the  
788 porous network in this deeper region with a highly tortuous and anisotropic porous network  
789 (Fig. 1) that was not preserved as ballistics but pulverised into ash is likely to have exhibited  
790 the most favourable conditions for large-scale pore overpressure during gas fluxing, resulting  
791 in the fragmentation and explosive eruption of the magma plugs. Based on the data presented  
792 in this paper, we propose that the timescale for this large-scale overpressure development may  
793 have been controlled by the permeability of the most degassed portion of the plug, which was  
794 dependent on the crystal micro-textures dictated by changing decompression rates, which may  
795 have exerted a rheological control on densification rate.

796

## 797 **6. Conclusions**

798

799 We have combined an experimental determination of the connected porosity and gas  
800 permeability of ballistic bombs produced by the 2004-2010 sequence of vulcanian explosions  
801 at Galeras volcano, Colombia, with micro-tomographic reconstructions of the porous micro-  
802 structures to illustrate the changes in the porous network that occur as a result of the  
803 densification of high-crystallinity andesitic magma plugs. Densification results in the reduction  
804 of mean pore volumes and mean throat areas, as well as a reduction in the volumetric number  
805 density of pores and throats. We observe a relative loss of throats compared to pores and a  
806 decline of disconnected voids with reducing porosity, suggesting progressive pore closure  
807 and/or coalescence of isolated pores to the connected network. These micro-structural changes  
808 produced a reduction in tortuosity of the permeable pathways during magma densification,  
809 enabling the development of a plug without the large-scale development of gas overpressure

810 owing to the retention of permeability to low levels of connected porosity. In contrast, magma  
811 residing at deeper levels below densifying plugs is characterised by large pore volumes and  
812 pore throat areas, but the high variance of these properties and the high tortuosity and  
813 anisotropy of the porous network suggest that pore overpressure may be more likely to develop  
814 at these deeper levels in the conduit, providing the driving force for vulcanian explosions. In  
815 combination with previously-published crystal micro-texture and groundmass glass volatile  
816 data, the porous micro-structure data presented here argues for a plug formation model where  
817 variations in densification rate and final permeability are controlled by variations in crystal  
818 micro-textures. The extent of densification, plug permeability and plug degassing may  
819 therefore be ultimately controlled by magma decompression and ascent rates, which control  
820 the variations in crystal micro-textures that modulate magma rheology and densification rate.  
821 Building understanding of the links between magma ascent rates, crystal micro-textures, bulk  
822 magma rheology and densification processes may therefore provide important insights into  
823 vulcanian eruption explosivity.

824

## 825 **Acknowledgements**

826 This work was funded by a Natural Environment Research Council Doctoral Training  
827 Partnership grant [NE/L002558/1] to A. Bain. Y. Lavallée, A. Lamur and the Experimental  
828 Volcanology and Geothermal Research Laboratory at the University of Liverpool were  
829 supported by a starting grant of the European Research Council (ERC) on Strain Localisation  
830 in Magma [SLiM; no. 306488]. J. E. Kendrick was supported by an Early Career Fellowship  
831 of the Leverhulme Trust. A. Bain thanks Wim Degruyter for kindly sharing the 3DMA-Rock  
832 code and providing advice on implementation, and Rebekah Harries for helpful discussions.  
833 The authors thank two anonymous reviewers for their helpful and constructive comments, and  
834 Heidy Mader for editorial handling.

835

836 **Competing Interests Statement**

837 The authors declare no competing interests.

838

839 **References**

840

841 Ashwell, P.A., Kendrick, J.E., Lavallée, Y., Kennedy, B.M., Hess, K.U., Von Aulock, F.W.,  
842 Wadsworth, F.B., Vasseur, J., Dingwell, D.B., 2015. Permeability of compacting porous  
843 lavas. *J. Geophys. Res. B Solid Earth* 120, 1605–1622.  
844 <https://doi.org/10.1002/2014JB011519>

845 Bai, T.B., Koster van Groos, A.F., 1994. Diffusion of chlorine in granitic melts. *Geochim.*  
846 *Cosmochim. Acta* 58, 113–123. [https://doi.org/10.1016/0016-7037\(94\)90450-2](https://doi.org/10.1016/0016-7037(94)90450-2)

847 Bain, A.A., Calder, E.S., Cortés, J.A., Cortés, G.P., Loughlin, S., 2019. Textural and  
848 geochemical constraints on andesitic plug emplacement prior to the 2004-2010  
849 vulcanian explosions at Galeras volcano, Colombia. *Bull. Volcanol.* 81, 1.

850 Bear, J., 1972. *Dynamics of fluids in porous media*. American Elsevier Publishing Co. Inc.,  
851 New York.

852 Berkowitz, B., 2002. Characterizing flow and transport in fractured geological media: A  
853 review. *Adv. Water Resour.* 25, 861–884. [https://doi.org/10.1016/S0309-](https://doi.org/10.1016/S0309-1708(02)00042-8)  
854 [1708\(02\)00042-8](https://doi.org/10.1016/S0309-1708(02)00042-8)

855 Berlo, K., Tuffen, H., Smith, V.C., Castro, J.M., Pyle, D.M., Mather, T.A., Geraki, K., 2013.  
856 Element variations in rhyolitic magma resulting from gas transport. *Geochim.*  
857 *Cosmochim. Acta* 121, 436–451. <https://doi.org/10.1016/j.gca.2013.07.032>

858 Bernabé, Y., Bruderer, C., 1998. Effect of the variance of pore size distribution on the  
859 transport properties of heterogeneous networks. *J. Geophys. Res. Solid Earth* 103, 513–  
860 525. <https://doi.org/10.1029/97JB02486>

861 Bernabé, Y., Mok, U., Evans, B., 2003. Permeability-porosity relationships in rocks subjected  
862 to various evolution processes. *Pure Appl. Geophys.* 160, 937–960.  
863 <https://doi.org/10.1007/PL00012574>

864 Bernard, M.L., Zamora, M., Géraud, Y., Boudon, G., 2007. Transport properties of  
865 pyroclastic rocks from Montagne Pelée volcano (Martinique, Lesser Antilles). *J.*  
866 *Geophys. Res. Solid Earth* 112, 1–16. <https://doi.org/10.1029/2006JB004385>

867 Blower, J., 2001. Factors controlling permeability-porosity relationships in magma. *Bull.*  
868 *Volcanol.* 63, 497–504. <https://doi.org/10.1007/s004450100172>

869 Browning, J., Meredith, P., Gudmundsson, A., 2016. Cooling-dominated cracking in  
870 thermally stressed volcanic rocks. *Geophys. Res. Lett.* 43, 8417–8425.  
871 <https://doi.org/10.1002/2016GL070532>

872 Brugger, C.R., Hammer, J.E., 2010. Crystallization kinetics in continuous decompression  
873 experiments: Implications for interpreting natural magma ascent processes. *J. Petrol.* 51,  
874 1941–1965. <https://doi.org/10.1093/petrology/egq044>

875 Burgisser, A., Chevalier, L., Gardner, J.E., Castro, J.M., 2017. The percolation threshold and  
876 permeability evolution of ascending magmas. *Earth Planet. Sci. Lett.* 470, 37–47.  
877 <https://doi.org/10.1016/j.epsl.2017.04.023>

878 Cashman, K., Blundy, J., 2000. Degassing and crystallization of ascending andesite and  
879 dacite. *Philos. Trans. R. Soc. London A Math. Phys. Eng. Sci.* 358, 1487–1513.

880 Cassidy, M., Manga, M., Cashman, K., Bachmann, O., 2018. Controls on explosive-effusive  
881 volcanic eruption styles. *Nat. Commun.* 9, 2839. <https://doi.org/10.1038/s41467-018->

882 05293-3

- 883 Castro, J.M., Bindeman, I.N., Tuffen, H., Ian Schipper, C., 2014. Explosive origin of silicic  
884 lava: Textural and delta-H<sub>2</sub>O evidence for pyroclastic degassing during rhyolite effusion.  
885 Earth Planet. Sci. Lett. 405, 52–61. <https://doi.org/10.1016/j.epsl.2014.08.012>
- 886 Castro, J.M., Cordonnier, B., Tuffen, H., Tobin, M.J., Puskar, L., Martin, M.C., Bechtel,  
887 H.A., 2012. The role of melt-fracture degassing in defusing explosive rhyolite eruptions  
888 at volcan Chaitén. Earth Planet. Sci. Lett. 333–334, 63–69.  
889 <https://doi.org/10.1016/j.epsl.2012.04.024>
- 890 Clarke, A.B., 2013. Unsteady explosive activity: vulcanian eruptions, in: Fagents, S.A.,  
891 Gregg, T.K.P., Lopes, R.M.C. (Eds.), *Modeling Volcanic Processes: The Physics and*  
892 *Mathematics of Volcanism*. Cambridge University Press.
- 893 Clarke, A.B., Stephens, S., Teasdale, R., Sparks, R.S.J., Diller, K., 2007. Petrologic  
894 constraints on the decompression history of magma prior to Vulcanian explosions at the  
895 Soufrière Hills volcano, Montserrat. *J. Volcanol. Geotherm. Res.* 161, 261–274.  
896 <https://doi.org/10.1016/j.jvolgeores.2006.11.007>
- 897 Coats, R., Kendrick, J.E., Wallace, P.A., Miwa, T., Hornby, A.J., Ashworth, J.D.,  
898 Matsushima, T., Lavallée, Y., 2018. Failure criteria for porous dome rocks and lavas: a  
899 study of Mt. Unzen, Japan. *Solid Earth Discuss.* <https://doi.org/10.5194/se-2018-19>
- 900 Colombier, M., Wadsworth, F.B., Gurioli, L., Scheu, B., Kueppers, U., Di Muro, A.,  
901 Dingwell, D.B., 2017. The evolution of pore connectivity in volcanic rocks. *Earth*  
902 *Planet. Sci. Lett.* 462, 99–109. <https://doi.org/10.1016/j.epsl.2017.01.011>
- 903 Costa, A., 2006. Permeability-porosity relationship: A reexamination of the Kozeny-Carman  
904 equation based on a fractal pore-space geometry assumption. *Geophys. Res. Lett.* 33, 1–  
905 5. <https://doi.org/10.1029/2005GL025134>

906 Darcy, H., 1857. Recherches expérimentales relatives au mouvement de l'eau dans les  
907 tuyaux. Mallet-Bachelier.

908 Darcy, H., 1856. Les fontaines publiques de la ville de Dijon: exposition et application...  
909 Victor Dalmont.

910 Degruyter, W., Bachmann, O., Burgisser, A., 2010. Controls on magma permeability in the  
911 volcanic conduit during the climactic phase of the Kos Plateau Tuff eruption (Aegean  
912 Arc). *Bull. Volcanol.* 72, 63–74. <https://doi.org/10.1007/s00445-009-0302-x>

913 Dierick, M., Masschaele, B., Van Hoorebeke, L., 2004. Octopus, a fast and user-friendly  
914 tomographic reconstruction package developed in LabView. *Meas. Sci. Technol.* 15,  
915 1366–1370. <https://doi.org/10.1088/0957-0233/15/7/020>

916 Dingwell, D., 1996. Volcanic dilemma: flow or blow? *Science* (80-. ). 273, 1054–1055.

917 Doyen, P.M., 1988. Permeability, conductivity, and pore geometry of sandstone. *J. Geophys.*  
918 *Res.* 93, 7729–7740. <https://doi.org/10.1029/JB093iB07p07729>

919 Eichelberger, J., Carrigan, C., Westrich, H., Price, R., 1986. Non-explosive silicic volcanism.  
920 *Nature* 323, 598–602.

921 Farquharson, J., Heap, M.J., Varley, N.R., Baud, P., Reuschle, T., 2015. Permeability and  
922 porosity relationships of edifice-forming andesites: A combined field and laboratory  
923 study. *J. Volcanol. Geotherm. Res.* 297, 52–68.  
924 <https://doi.org/10.1016/j.jvolgeores.2015.03.016>

925 Farquharson, J.I., Heap, M.J., Lavallée, Y., Varley, N.R., Baud, P., 2016. Evidence for the  
926 development of permeability anisotropy in lava domes and volcanic conduits. *J.*  
927 *Volcanol. Geotherm. Res.* 323, 163–185.  
928 <https://doi.org/10.1016/j.jvolgeores.2016.05.007>

929 Giachetti, T., Druitt, T.H., Burgisser, A., Arbaret, L., Galven, C., 2010. Bubble nucleation,  
930 growth and coalescence during the 1997 Vulcanian explosions of Soufrière Hills  
931 Volcano, Montserrat. *J. Volcanol. Geotherm. Res.* 193, 215–231.  
932 <https://doi.org/10.1016/j.jvolgeores.2010.04.001>

933 Gonnermann, H.M., Giachetti, T., Fliedner, C., Nguyen, C.T., Houghton, B.F., Crozier, J.A.,  
934 Carey, R.J., 2017. Permeability During Magma Expansion and Compaction. *J. Geophys.*  
935 *Res. Solid Earth* 122, 9825–9848. <https://doi.org/10.1002/2017JB014783>

936 Hammer, J.E., Cashman, K.V., Voight, B., 2000. Magmatic processes revealed by textural  
937 and compositional trends in Merapi dome lavas. *J. Volcanol. Geotherm. Res.* 100, 165–  
938 192. [https://doi.org/10.1016/S0377-0273\(00\)00136-0](https://doi.org/10.1016/S0377-0273(00)00136-0)

939 Hammer, J.E., Cashman, K. V., Hoblitt, R.P., Newman, S., 1999. Degassing and microlite  
940 crystallization during pre-climactic events of the 1991 eruption of Mt. Pinatubo,  
941 Philippines. *Bull. Volcanol.* 60, 355–380. <https://doi.org/10.1007/s004450050238>

942 Heap, M.J., Farquharson, J.I., Wadsworth, F.B., Kolzenburg, S., Russell, J.K., 2015.  
943 Timescales for permeability reduction and strength recovery in densifying magma. *Earth*  
944 *Planet. Sci. Lett.* 429, 223–233. <https://doi.org/10.1016/j.epsl.2015.07.053>

945 Heap, M.J., Kennedy, B., 2016. Exploring the Scale-Dependent permeability of fractured  
946 andesite. *Earth Planet. Sci. Lett.* 447, 956–963.  
947 <https://doi.org/10.1017/CBO9781107415324.004>

948 Heap, M.J., Reuschlé, T., Farquharson, J.I., Baud, P., 2018. Permeability of volcanic rocks to  
949 gas and water. *J. Volcanol. Geotherm. Res.* 354, 29–38.  
950 <https://doi.org/10.1016/j.jvolgeores.2018.02.002>

951 Heap, M.J., Violay, M., Wadsworth, F.B., Vasseur, J., 2017. From rock to magma and back  
952 again: The evolution of temperature and deformation mechanism in conduit margin

953 zones. *Earth Planet. Sci. Lett.* 463, 92–100. <https://doi.org/10.1016/j.epsl.2017.01.021>

954 Hill, B.E., 1984. Petrology of the Bend pumice and Tumalo tuff, a Pleistocene Cascade  
955 eruption involving magma mixing.

956 Hoblitt, R.P., Harmon, R.S., 1993. Bimodal Density Distribution of Cryptodome Dacite from  
957 the 1980 Eruption of Mount St. Helens, Washington. *Bull. Volcanol.* 55, 421–437.  
958 <https://doi.org/10.1007/BF00302002>

959 Jouniaux, L., Bernard, M.-L., Zamora, M., Pozzi, J.-P., 2000. Streaming potential in volcanic  
960 rocks from Mount Peleé. *J. Geophys. Res.* 105, 8391–8401.  
961 <https://doi.org/10.1029/1999jb900435>

962 Kendrick, J.E., Lavallée, Y., Hess, K.U., Heap, M.J., Gaunt, H.E., Meredith, P.G., Dingwell,  
963 D.B., 2013. Tracking the permeable porous network during strain-dependent magmatic  
964 flow. *J. Volcanol. Geotherm. Res.* 260, 117–126.  
965 <https://doi.org/10.1016/j.jvolgeores.2013.05.012>

966 Kendrick, J.E., Lavallée, Y., Varley, N.R., Wadsworth, F.B., Lamb, O.D., Vasseur, J., 2016.  
967 Blowing Off Steam: Tuffisite Formation As a Regulator for Lava Dome Eruptions.  
968 *Front. Earth Sci.* 4, 1–15. <https://doi.org/10.3389/feart.2016.00041>

969 Kennedy, B.M., Wadsworth, F.B., Vasseur, J., Ian Schipper, C., Mark Jellinek, A., von  
970 Aulock, F.W., Hess, K.-U., Kelly Russell, J., Lavallée, Y., Nichols, A.R.L., Dingwell,  
971 D.B., 2016. Surface tension driven processes densify and retain permeability in magma  
972 and lava. *Earth Planet. Sci. Lett.* 433, 116–124.  
973 <https://doi.org/10.1016/j.epsl.2015.10.031>

974 Klein, J., Mueller, S.P., Helo, C., Gurioli, L., Castro, J.M., 2018. An expanded model and  
975 application of the combined effect of crystal-size distribution and crystal shape on the  
976 relative viscosity of magmas. *J. Volcanol. Geotherm. Res.* 357, 128–133.

977 <https://doi.org/10.1016/j.jvolgeores.2018.04.018>

978 Klinkenberg, L., 1941. The permeability of porous media to liquids and gases, in: *Drilling*  
979 *and Production Practice*.

980 Klug, C., Cashman, K. V., 1996. Permeability development in vesiculating magmas:  
981 implications for fragmentation. *Bull. Volcanol.* 58, 87–100.  
982 <https://doi.org/10.1007/s004450050128>

983 Kolzenburg, S., Heap, M.J., Lavallée, Y., Russell, J.K., Meredith, P.G., Dingwell, D.B.,  
984 2012. Strength and permeability recovery of tuffisite-bearing andesite. *Solid Earth* 3,  
985 191–198. <https://doi.org/10.5194/se-3-191-2012>

986 Kushnir, A.R.L., Martel, C., Champallier, R., Wadsworth, F.B., 2017. Permeability Evolution  
987 in Variably Glassy Basaltic Andesites Measured Under Magmatic Conditions. *Geophys.*  
988 *Res. Lett.* 44, 10,262-10,271. <https://doi.org/10.1002/2017GL074042>

989 Lamur, A., Kendrick, J.E., Eggertsson, G.H., Wall, R.J., Ashworth, J.D., Lavallée, Y., 2017.  
990 The permeability of fractured rocks in pressurised volcanic and geothermal systems. *Sci.*  
991 *Rep.* 7, 1–9. <https://doi.org/10.1038/s41598-017-05460-4>

992 Lamur, A., Kendrick, J.E., Wadsworth, F.B., Lavallée, Y., 2019. Fracture healing and  
993 strength recovery in magmatic liquids. *Geology* 47, 1–4.  
994 <https://doi.org/10.1130/G45512.1>

995 Lamur, A., Lavallée, Y., Iddon, F.E., Hornby, A.J., Kendrick, J.E., Von Aulock, F.W.,  
996 Wadsworth, F.B., 2018. Disclosing the temperature of columnar jointing in lavas. *Nat.*  
997 *Commun.* 9. <https://doi.org/10.1038/s41467-018-03842-4>

998 Laumonier, M., Arbaret, L., Burgisser, A., Champallier, R., 2011. Porosity redistribution  
999 enhanced by strain localization in crystal-rich magmas. *Geology* 39, 715–718.  
1000 <https://doi.org/10.1130/G31803.1>

1001 Lavallée, Y., Benson, P.M., Heap, M.J., Hess, K.U., Flaws, A., Schillinger, B., Meredith,  
1002 P.G., Dingwell, D.B., 2013. Reconstructing magma failure and the degassing network of  
1003 domebuilding eruptions. *Geology* 41, 515–518. <https://doi.org/10.1130/G33948.1>

1004 Lavallée, Y., Varley, N.R., Alatorre-Ibargüengoitia, M.A., Hess, K.U., Kueppers, U.,  
1005 Mueller, S., Richard, D., Scheu, B., Spieler, O., Dingwell, D.B., 2012. Magmatic  
1006 architecture of dome-building eruptions at Volcán de Colima, Mexico. *Bull. Volcanol.*  
1007 74, 249–260. <https://doi.org/10.1007/s00445-011-0518-4>

1008 Lee, T.-C., Kashyap, R.L., Chu, C.-N., 1994. Building skeleton models via 3-D medial  
1009 surface/axis thinning algorithms. *CVGIP Graph. Model. image Process.* 56, 462–478.

1010 Lindoo, A., Larsen, J.F., Cashman, K. V., Oppenheimer, J., 2017. Crystal controls on  
1011 permeability development and degassing in basaltic andesite magma. *Geology* 45, 831–  
1012 834. <https://doi.org/10.1130/G39157.1>

1013 Lindquist, W.B., Venkatarangan, A., 1999. Investigating 3D geometry of porous media from  
1014 high resolution images. *Phys. Chem. Earth, Part A Solid Earth Geod.* 24, 593–599.  
1015 [https://doi.org/10.1016/S1464-1895\(99\)00085-X](https://doi.org/10.1016/S1464-1895(99)00085-X)

1016 Matthäi, S.K., Belayneh, M., 2004. Fluid flow partitioning between fractures and a permeable  
1017 rock matrix. *Geophys. Res. Lett.* 31, 1–5. <https://doi.org/10.1029/2003GL019027>

1018 Michaut, C., Bercovici, D., Sparks, R.S.J., 2009. Ascent and compaction of gas rich magma  
1019 and the effects of hysteretic permeability. *Earth Planet. Sci. Lett.* 282, 258–267.  
1020 <https://doi.org/10.1016/j.epsl.2009.03.026>

1021 Mueller, S., Melnik, O., Spieler, O., Scheu, B., Dingwell, D.B., 2005. Permeability and  
1022 degassing of dome lavas undergoing rapid decompression: An experimental  
1023 determination. *Bull. Volcanol.* 67, 526–538. <https://doi.org/10.1007/s00445-004-0392-4>

1024 Oh, W., Lindquist, B.W., 1999. Image thresholding by indicator kriging. *IEEE Trans. Pattern*

1025 Anal. Mach. Intell. 21, 590–602. <https://doi.org/10.1109/34.777370>

1026 Okumura, S., Nakamura, M., Takeuchi, S., Tsuchiyama, A., Nakano, T., Uesugi, K., 2009.

1027 Magma deformation may induce non-explosive volcanism via degassing through bubble

1028 networks. *Earth Planet. Sci. Lett.* 281, 267–274.

1029 <https://doi.org/10.1016/j.epsl.2009.02.036>

1030 Okumura, S., Nakamura, M., Uesugi, K., Nakano, T., Fujioka, T., 2013. Coupled effect of

1031 magma degassing and rheology on silicic volcanism. *Earth Planet. Sci. Lett.* 362, 163–

1032 170. <https://doi.org/10.1016/j.epsl.2012.11.056>

1033 Okumura, S., Sasaki, O., 2014. Permeability reduction of fractured rhyolite in volcanic

1034 conduits and its control on eruption cyclicity. *Geology* 42, 843–846.

1035 <https://doi.org/10.1130/G35855.1>

1036 Preece, K., Gertisser, R., Barclay, J., Charbonnier, S.J., Komorowski, J.-C., Herd, R.A., 2016.

1037 Transitions between explosive and effusive phases during the cataclysmic 2010 eruption

1038 of Merapi volcano, Java, Indonesia. *Bull. Volcanol.* 78, 54.

1039 <https://doi.org/10.1007/s00445-016-1046-z>

1040 Rink, B.Y.M., 1976. Pore Structure and Physical Properties of Porous Sedimentary Rocks

1041 114.

1042 Rust, a. C., Cashman, K.V., Wallace, P.J., 2004. Magma degassing buffered by vapor flow

1043 through brecciated conduit margins. *Geology* 32, 349. <https://doi.org/10.1130/G20388.2>

1044 Rust, A.C., Cashman, K.V., 2004. Permeability of vesicular silicic magma: inertial and

1045 hysteresis effects. *Earth Planet. Sci. Lett.* 228, 93–107.

1046 <https://doi.org/10.1016/j.epsl.2004.09.025>

1047 Saar, M.O., Manga, M., 1999. Permeability-porosity relationships in vesicular basalts.

1048 *Geophys. Res. Lett.* 26, 111–114.

1049 Sato, H., Fujii, T., Nakada, S., 1992. Crumbling of dacite dome lava and generation of  
1050 pyroclastic flows at Unzen volcano. *Nature* 360, 664–666.

1051 Saubin, E., Tuffen, H., Gurioli, L., Owen, J., Castro, J.M., Berlo, K., McGowan, E.M.,  
1052 Schipper, C.I., Wehbe, K., 2016. Conduit Dynamics in Transitional Rhyolitic Activity  
1053 Recorded by Tuffsite Vein Textures from the 2008–2009 Chaitén Eruption. *Front. Earth*  
1054 *Sci.* 4. <https://doi.org/10.3389/feart.2016.00059>

1055 Schneider, C.A., Rasband, W.S., Eliceiri, K.W., 2012. NIH Image to ImageJ: 25 years of  
1056 image analysis. *Nat. Methods* 9, 671–675. <https://doi.org/10.1038/nmeth.2089>

1057 Silver, L.A., Ihinger, P.D., Stolper, E., 1990. The influence of bulk composition on the  
1058 speciation of water in silicate glasses. *Contrib. to Mineral. Petrol.* 104, 142–162.  
1059 <https://doi.org/10.1007/BF00306439>

1060 Sparks, R.S.J., 1997. Causes and consequences of pressurisation in lava dome eruptions.  
1061 *Earth Planet. Sci. Lett.* 150, 177–189. [https://doi.org/10.1016/S0012-821X\(97\)00109-X](https://doi.org/10.1016/S0012-821X(97)00109-X)

1062 Stix, J., Calvache, M., Fischer, T., Gómez, D., 1993. A model of degassing at Galeras  
1063 Volcano, Colombia, 1988-1993. *Geology* 21, 963–967. [https://doi.org/10.1130/0091-](https://doi.org/10.1130/0091-7613(1993)021<0963)  
1064 [7613\(1993\)021<0963](https://doi.org/10.1130/0091-7613(1993)021<0963)

1065 Stix, J., Torres, R.C., Medina, L.N., Cortés, G.P., Raigosa, J.A., Gómez, D., Castonguay, R.,  
1066 1997. A model of vulcanian eruptions at Galeras volcano, Colombia. *J. Volcanol.*  
1067 *Geotherm. Res.* 77, 285–303.

1068 Tait, M.A., 2004. Dynamics of a large volume plinian eruption: dispersal of the late Miocene  
1069 Corte Blanco tuff, Ramadas Volcanic Centre, Andes Mountains, Salta, Argentina.  
1070 Monash University.

1071 Takeuchi, S., Nakashima, S., Tomiya, A., Shinohara, H., 2005. Experimental constraints on  
1072 the low gas permeability of vesicular magma during decompression. *Geophys. Res. Lett.*

1073 32, 1–5. <https://doi.org/10.1029/2005GL022491>

1074 Tuffen, H., Dingwell, D.B., Pinkerton, H., 2003. Repeated fracture and healing of silicic  
1075 magma generate flow banding and earthquakes? *Geology* 31, 1089–1092.  
1076 <https://doi.org/10.1130/G19777.1>

1077 Voight, B., 1999. Magma Flow Instability and Cyclic Activity at Soufriere Hills Volcano,  
1078 Montserrat, British West Indies. *Science* (80-. ). 283, 1138–1142.

1079 Wadsworth, F.B., Vasseur, J., Llewellyn, E.W., Dobson, K.J., Colombier, M., Von Aulock,  
1080 F.W., Fife, J.L., Wiesmaier, S., Hess, K.U., Scheu, B., Lavallée, Y., Dingwell, D.B.,  
1081 2017. Topological inversions in coalescing granular media control fluid-flow regimes.  
1082 *Phys. Rev. E* 96, 1–6. <https://doi.org/10.1103/PhysRevE.96.033113>

1083 Wadsworth, F.B., Vasseur, J., Scheu, B., Kendrick, J.E., Lavallée, Y., Dingwell, D.B., 2016.  
1084 Universal scaling of fluid permeability during volcanic welding and sediment  
1085 diagenesis. *Geology* 44, 219–222. <https://doi.org/10.1130/G37559.1>

1086 Whitaker, S., 1996. The Forchheimer equation: A theoretical development. *Transp. Porous*  
1087 *Media* 25, 27–61. <https://doi.org/10.1007/BF00141261>

1088 Wright, H.M., Cashman, K. V., 2014. Compaction and gas loss in welded pyroclastic  
1089 deposits as revealed by porosity, permeability, and electrical conductivity measurements  
1090 of the Shevlin Park Tuff. *Bull. Geol. Soc. Am.* 126, 234–247.  
1091 <https://doi.org/10.1130/B30668.1>

1092 Wright, H.M.N., Cashman, K. V., Gottesfeld, E.H., Roberts, J.J., 2009. Pore structure of  
1093 volcanic clasts: Measurements of permeability and electrical conductivity. *Earth Planet.*  
1094 *Sci. Lett.* 280, 93–104. <https://doi.org/10.1016/j.epsl.2009.01.023>

1095 Wright, H.M.N., Cashman, K. V., Rosi, M., Cioni, R., 2007. Breadcrust bombs as indicators  
1096 of Vulcanian eruption dynamics at Guagua Pichincha volcano, Ecuador. *Bull. Volcanol.*

1097 69, 281–300.

1098 Wright, H.M.N., Roberts, J.J., Cashman, K. V., 2006. Permeability of anisotropic tube

1099 pumice: Model calculations and measurements. *Geophys. Res. Lett.* 33.

1100 <https://doi.org/10.1029/2006GL027224>

1101 Wright, H.M.N., Weinberg, R.F., 2009. Strain localization in vesicular magma: Implications

1102 for rheology and fragmentation. *Geology* 37, 1023–1026.

1103 <https://doi.org/10.1130/G30199A.1>

1104 Yokoyama, T., Takeuchi, S., 2009. Porosimetry of vesicular volcanic products by a water-

1105 expulsion method and the relationship of pore characteristics to permeability. *J.*

1106 *Geophys. Res. Solid Earth* 114. <https://doi.org/10.1029/2008JB005758>

1107 Zhu, W., Wong, F., 1996. *Damage and Tortuosity* 23, 3099–3102.

1108

1109

1110

1111

1112

1113

1114

1115

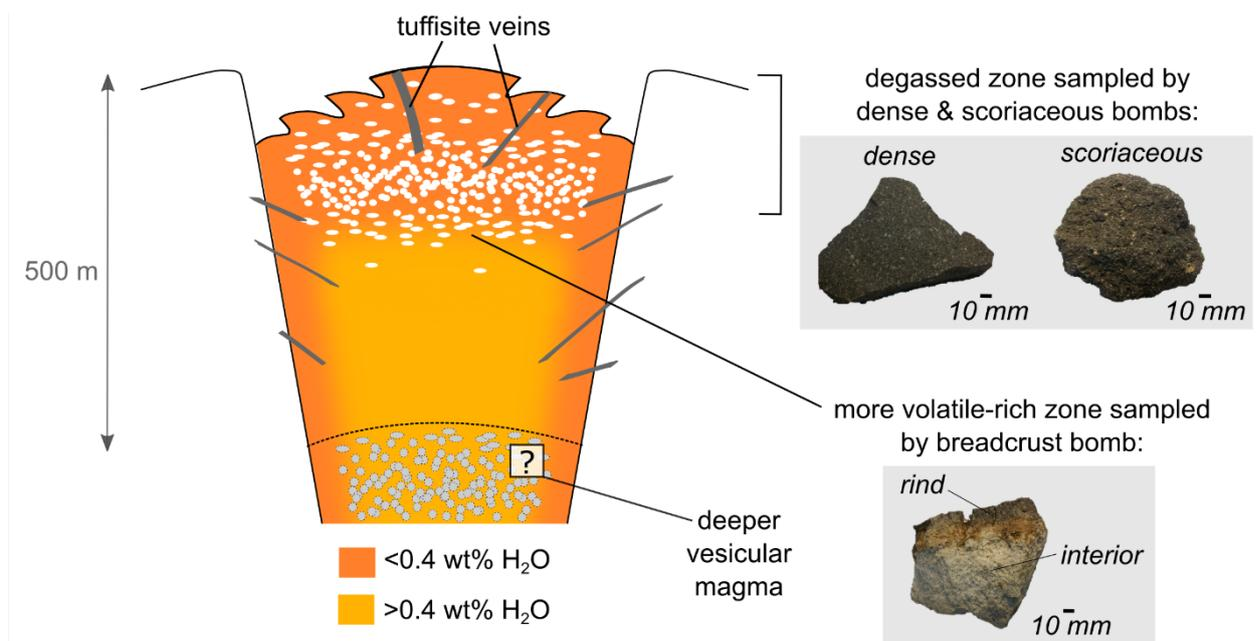
1116

1117

1118

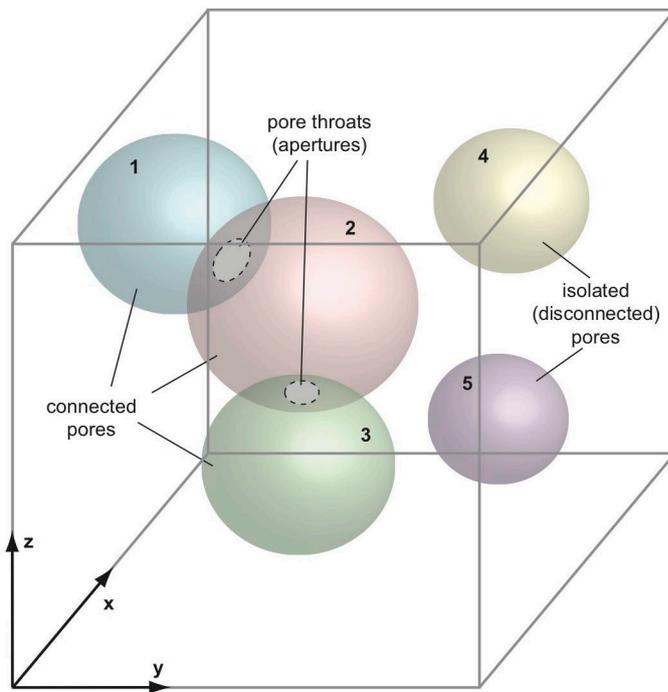
1119 **Figures :**

1120



1121

1122 **Fig. 1:** Structure of the average andesitic magma plug at Galeras volcano, modified from  
1123 Bain et al. (2019), showing the properties of the source areas for the three different bomb  
1124 types produced in the 2004-2010 vulcanian explosions. Dense and scoriaceous bombs were  
1125 typically sourced from no more than 100 m depth in the conduit. The breadcrust bomb shown  
1126 here is a fragment displaying the highly vesicular bomb interior resulting from syn-eruptive  
1127 vesiculation and the dense exterior rind representative of the pre-eruptive magma properties.  
1128 Dense and scoriaceous bombs did not experience syn-eruptive vesiculation and preserve the  
1129 pre-eruptive magma properties. Also shown is a hypothetical deeper zone of vesicular magma  
1130 (>500 m) that may represent the region where pore overpressure increased sufficiently to  
1131 drive vulcanian explosions (Bain et al. 2019).



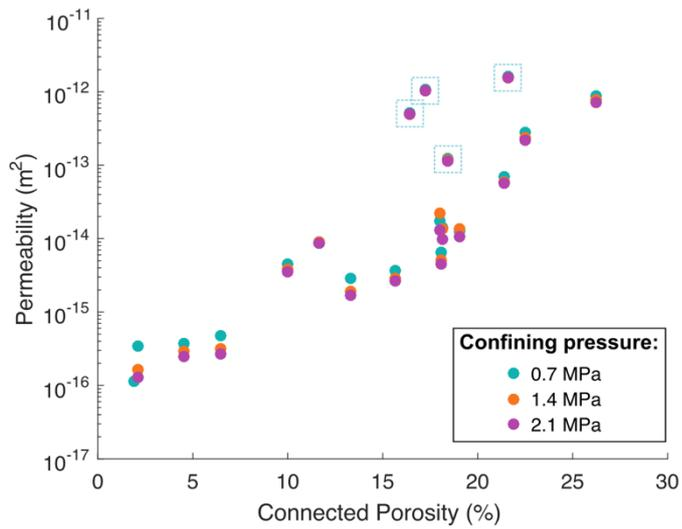
1132

1133 **Fig. 2:** Simplified illustration of the porous network analysed by micro-tomography (pores  
 1134 are not spherical in real samples, see Fig. 4 & 5). This example volume contains three  
 1135 connected pores (1, 2 & 3) and two pore throats, as well as two disconnected pores or voids  
 1136 (4 & 5). Pores 1 and 3 have a coordination number of 1 and pore 2 has a coordination number  
 1137 of 2. Connected and isolated pores were quantified as separate populations, giving volumetric  
 1138 number densities of connected pores and disconnected voids, as well as a volumetric number  
 1139 density of pore throats. The volumes of connected pores and isolated pores were also  
 1140 measured, as well as throat surface areas. Permeability was measured parallel to the z  
 1141 direction (see frame of reference).

1142

1143

1144

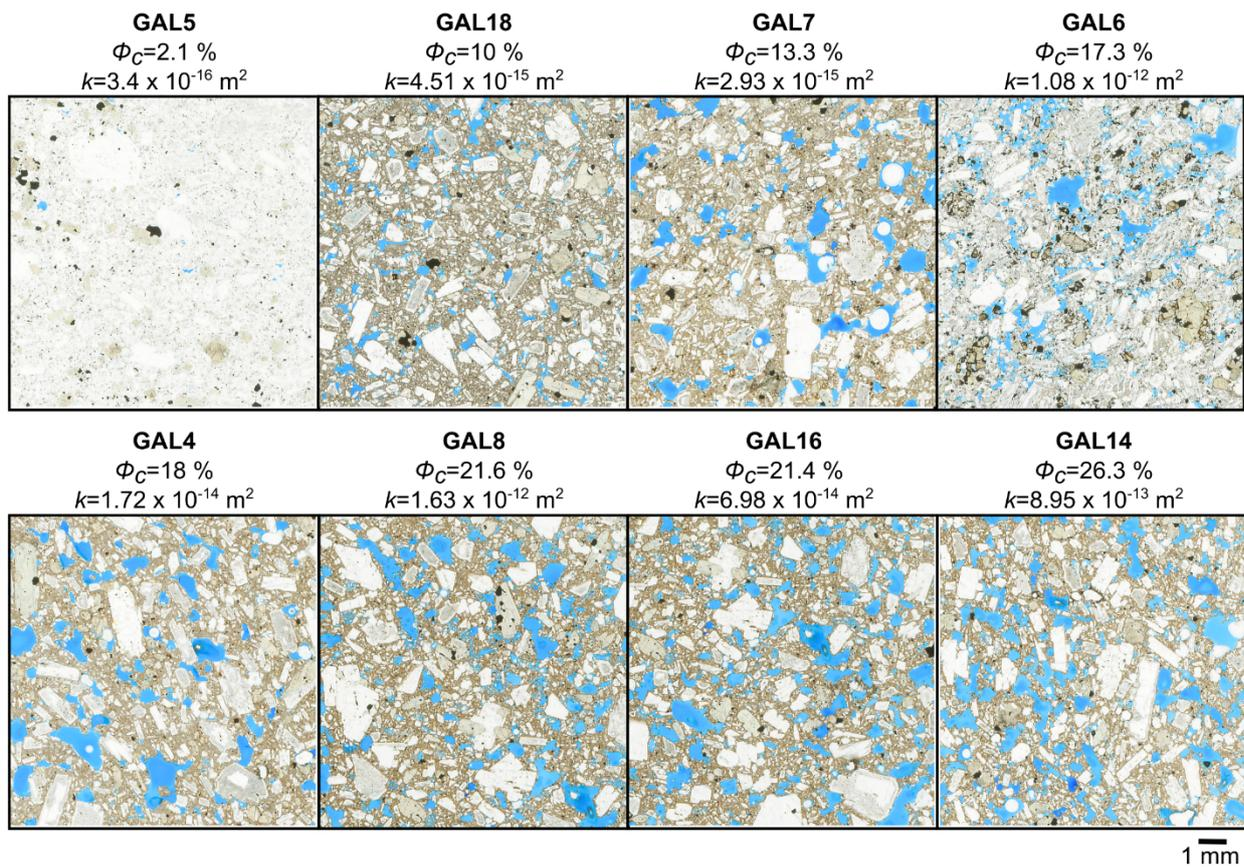


1145

1146 **Fig. 3:** Gas permeability varies from  $1.13 \times 10^{-16} - 1.63 \times 10^{-12} \text{ m}^2$  over the measured range  
 1147 of connected porosity (1.9-26.3 %) and the range of applied confining pressures (0.7-2.1  
 1148 MPa). Propagated errors for connected porosity and permeability measurements are smaller  
 1149 than the symbol size, see section 3.2. Permeability is lower in samples with lower connected  
 1150 porosity and permeability for each sample is lower at higher confining pressures. Dashed  
 1151 boxes indicate samples with higher permeability (GAL6, GAL8, GAL13, GAL19) than other  
 1152 samples with similar connected porosity, see section 4.1 and Table 1.

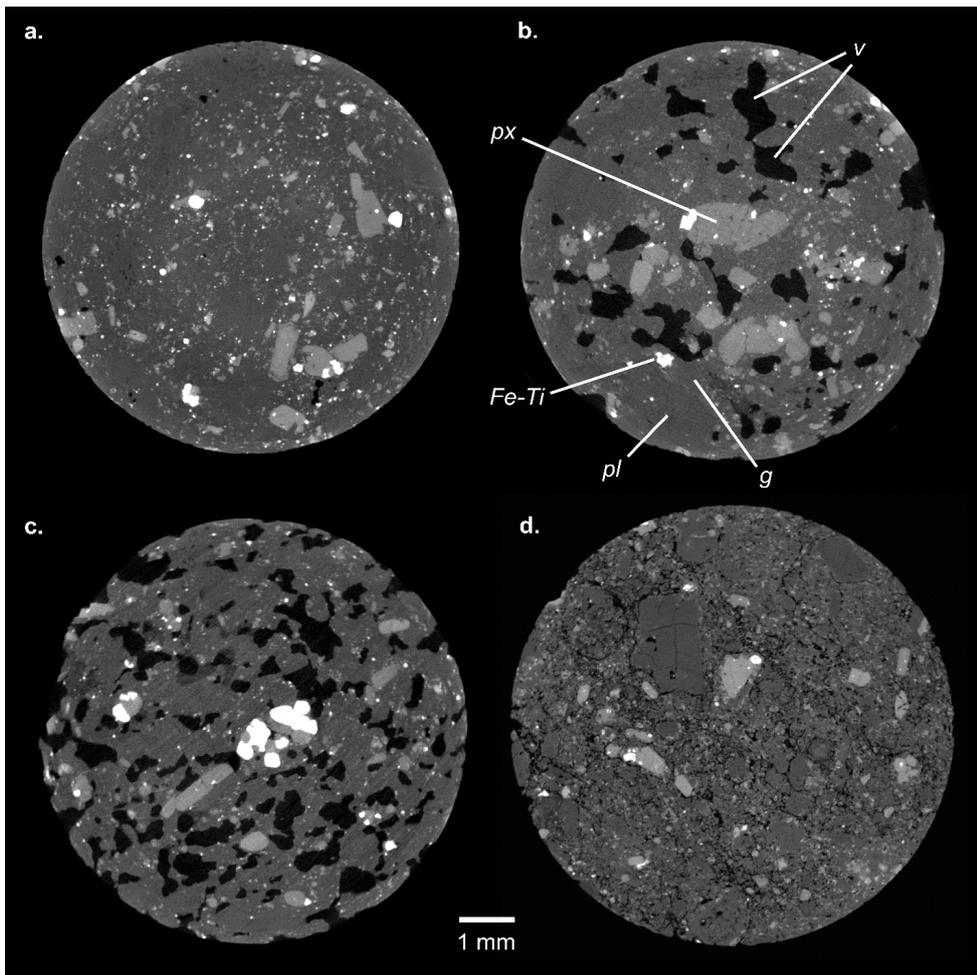
1153

1154



1155

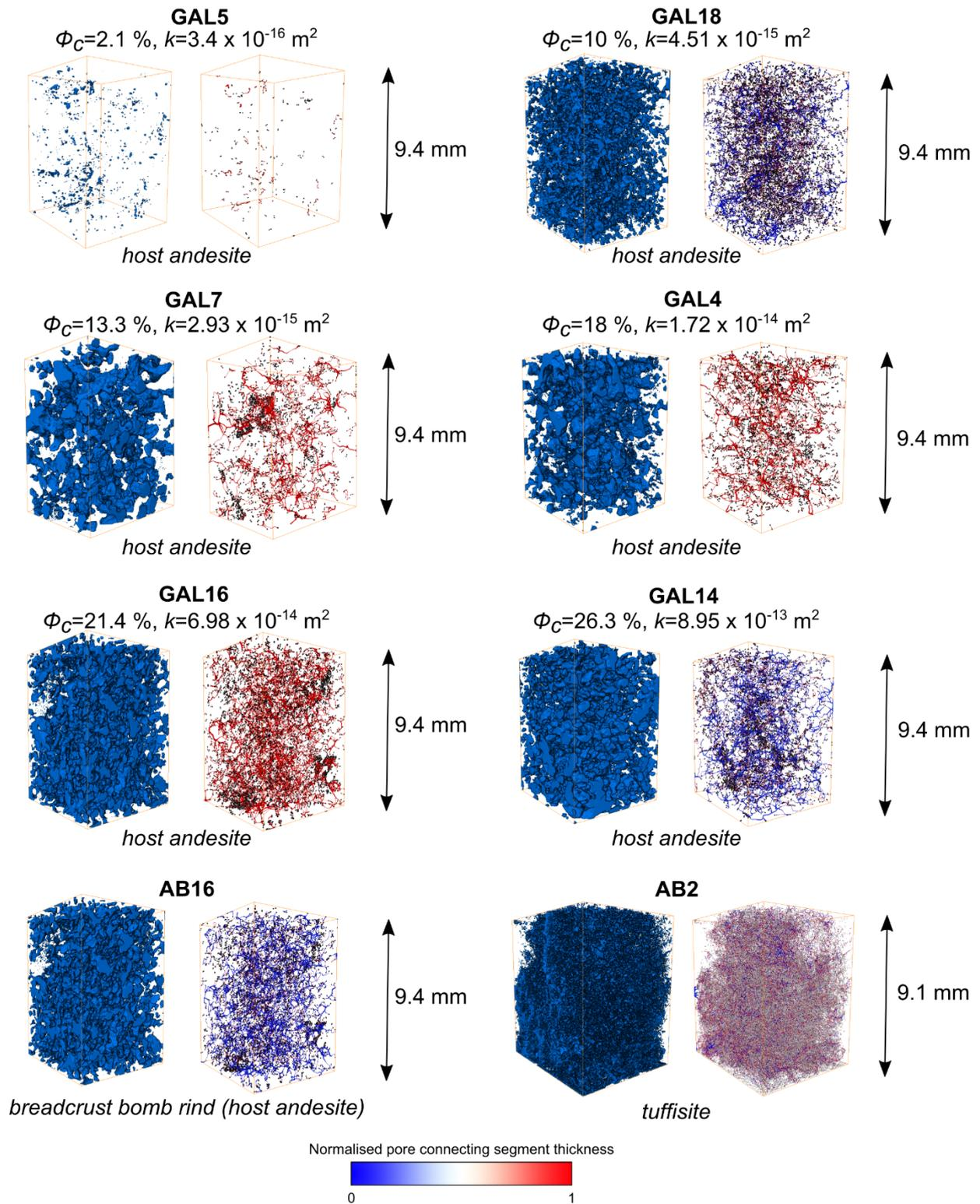
1156 **Fig. 4:** Scanned images of sample thin sections with increasing connected porosities  $\phi_c$ .  
 1157 Permeability,  $k$ , measured at 0.7 MPa confining pressure is also indicated. All samples are  
 1158 porphyritic andesite bombs. Voids are shown in blue epoxy resin with occasional rounded  
 1159 white air bubbles.



1160

1161 **Fig. 5:** Examples of reconstructed micro-tomographic slices of different types of samples,  
 1162 which constitute the X-ray micro-tomography data used to measure the properties of the  
 1163 porous network (numerical porosity, pore volumes, throat areas, number densities,  
 1164 tortuosity). Void space (*v*) appears black, plagioclase crystals (*pl*) and glassy groundmass (*g*)  
 1165 appear dark grey, pyroxene crystals (*px*) appear light grey and Fe-Ti oxide crystals (*Fe-Ti*)  
 1166 appear white. **a.** Dense host andesite featuring very few, small void spaces **b.** More porous  
 1167 host andesite showing large polylobate/branching pores **c.** Porous rind of the breadcrust  
 1168 bomb, also showing polylobate/branching pores **d.** Tuffisite sample showing a distinct pore  
 1169 structure characterised by curvilinear voids surrounding a granular solid fraction made up of  
 1170 rounded fragments of the host andesite phases.

1171



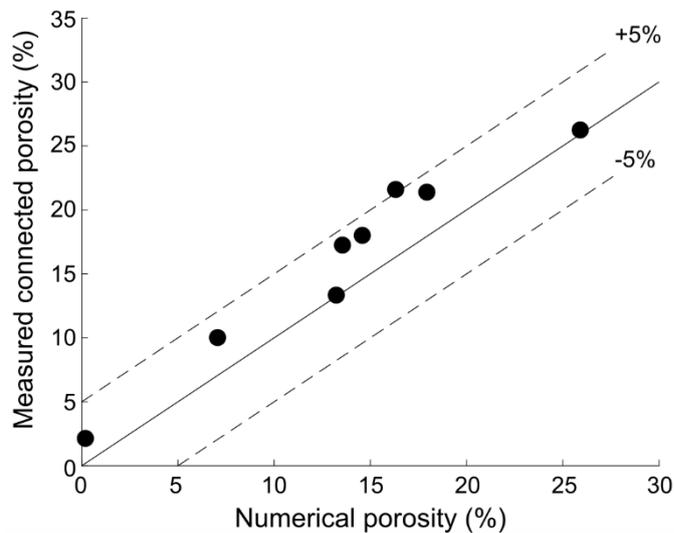
1172

1173 **Fig. 6:** Rendering of the segmented pore space (left) and pore network model (right) for  
 1174 selected samples covering a range of connected porosities. Segmentation and skeletonisation  
 1175 for the renderings shown here were performed using Avizo software v9, for illustration

1176 purposes only. All quantification of the pore space was performed using 3DMA-Rock  
1177 (Lindquist & Venkatarangan 1999). The height (measured in the z direction) of each data  
1178 volume is indicated by the black arrows. In the pore network models shown here, nodal pores  
1179 are illustrated by black spheres and segments joining nodal pores are shown with thicknesses  
1180 and colours normalised by the maximum distance from the skeleton to the exterior edge of  
1181 the pore space object (see colour bar). The connected porosity,  $\phi_c$ , and the permeability,  $k$ ,  
1182 (measured at a confining pressure of 0.7 MPa) are given for samples for which these were  
1183 measured.

1184

1185

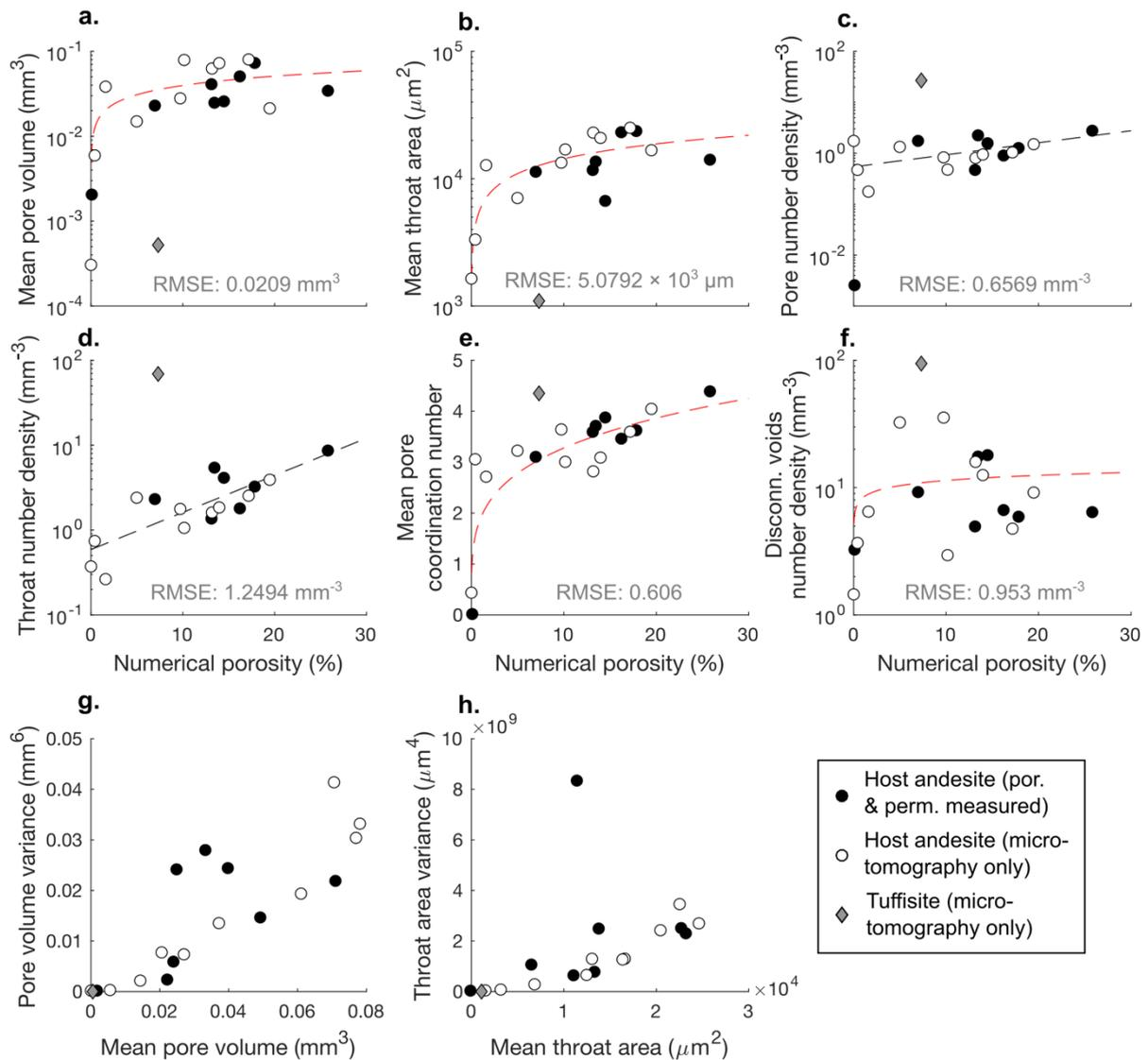


1186

1187

1188 **Fig. 7:** Comparison of connected porosity measured by pycnometry and total numerical  
1189 porosity calculated from micro-tomography data. The solid line represents the one-to-one  
1190 line, with +5 % and -5 % difference indicated by the dashed lines.

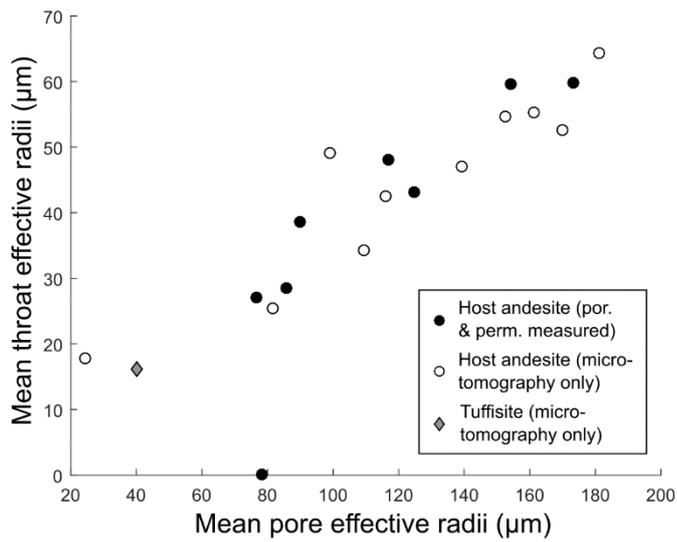
1191



1192

1193 **Fig. 8:** a–f Micro-tomography results compared with the total numerical porosity calculated  
 1194 for each sample. Dashed lines correspond to the least-squares best-fit power law (red) and  
 1195 exponential (black) functions to highlight overall relationships for the host andesite (RMSE  
 1196 indicated in each panel). Other attempted fits are given in Supplementary File A. Samples of  
 1197 host andesite with lower numerical porosity have smaller mean pore volumes and mean  
 1198 throat areas, lower volumetric number densities of connected pores, throats and disconnected  
 1199 voids, and smaller mean pore coordination numbers. **g–h** Samples with lower mean pore  
 1200 volumes and mean throat areas also have lower pore volume and throat area variances.

1201



1202

1203

**Fig. 9:** The mean pore and mean throat effective radii in each sample are positively

1204

correlated, showing that samples with small pores have small pore throats and vice-versa.

1205

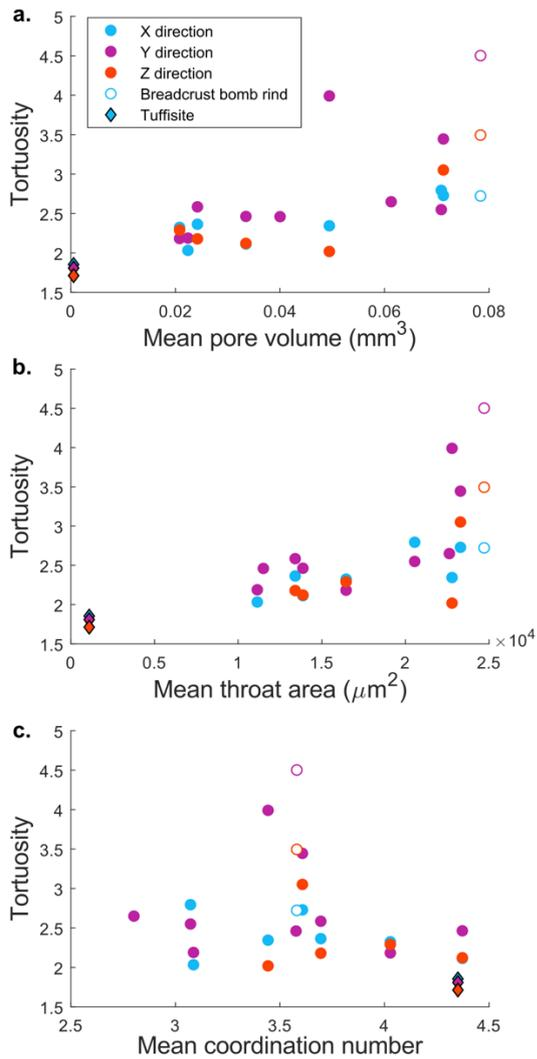
One clear outlier corresponds to dense sample GAL5, where only one pore and zero throats

1206

were identified by micro-tomography in the analysed volume after the data cleaning

1207

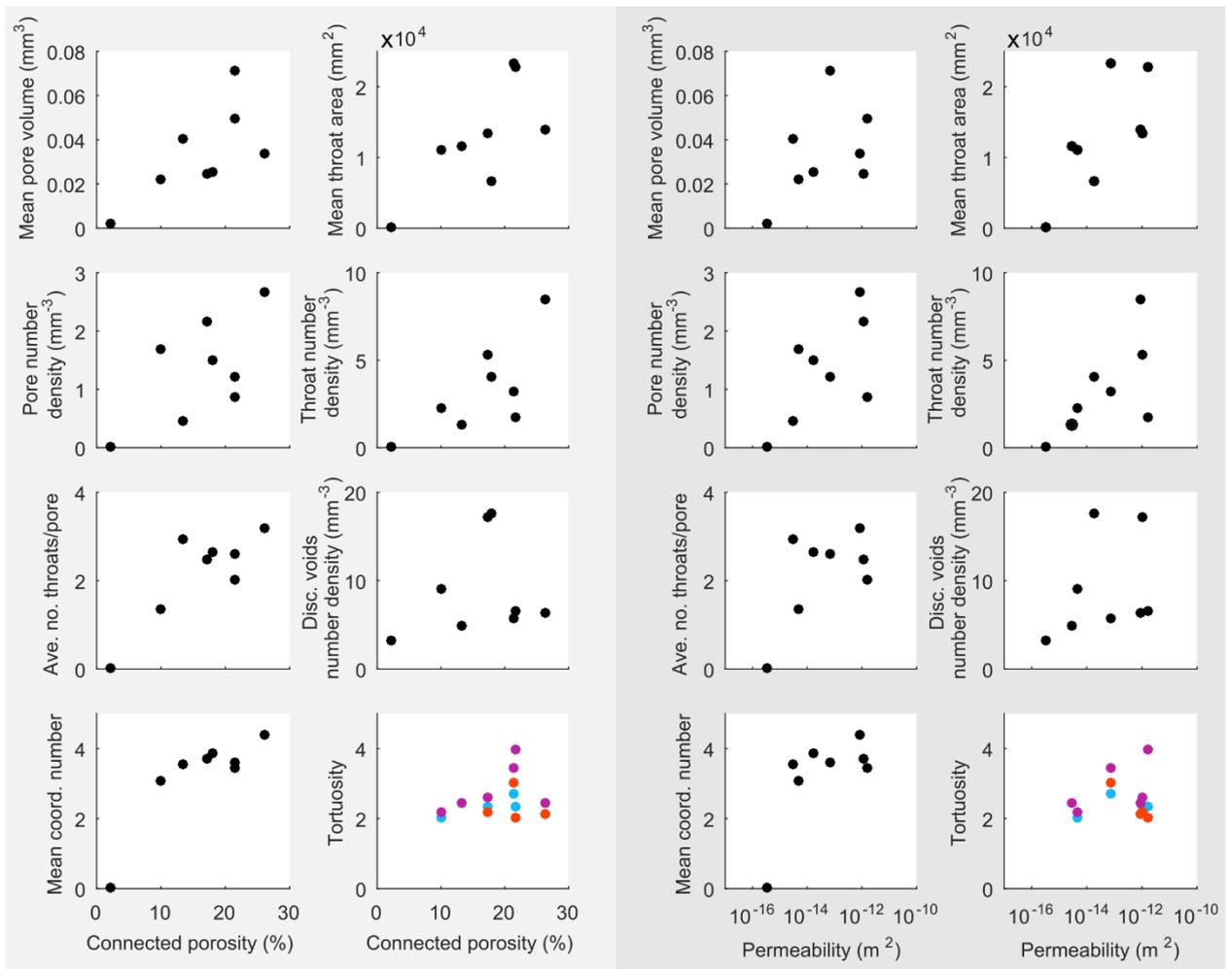
procedure.



1208

1209 **Fig. 10:** Median geometric tortuosity measured where possible along connected paths in each  
 1210 direction (x, y and z) of the prismatic volume analysed by micro-tomography. Diamonds  
 1211 correspond to the tuffisite sample and open symbols correspond to the breadcrust bomb rind.  
 1212 Tortuosity is typically lower and more isotropic in samples with lower mean pore volumes  
 1213 and lower mean throat areas. Tortuosity shows no clear relationship with mean pore  
 1214 coordination number. The tuffisite sample shows the lowest tortuosity in the dataset and the  
 1215 breadcrust bomb rind shows the highest anisotropy with respect to tortuosity.

1216



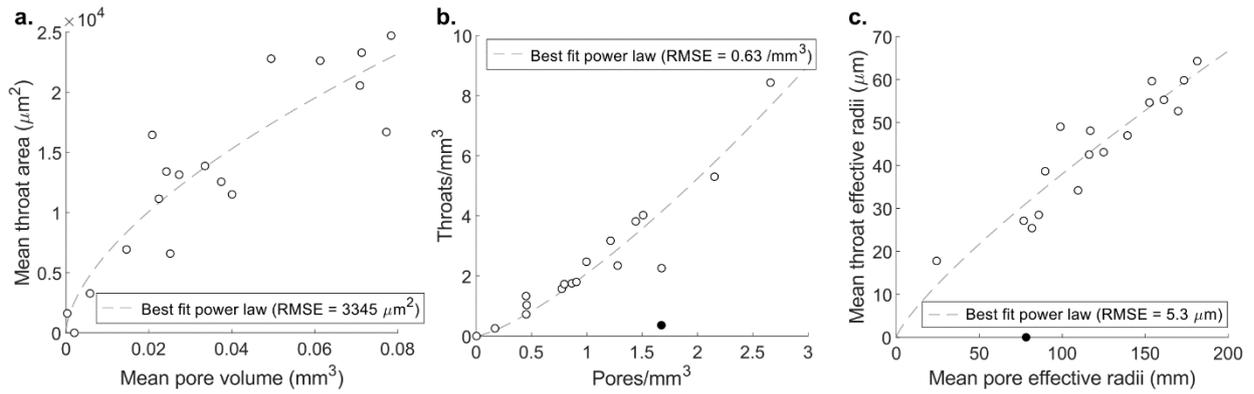
1217

1218 **Fig. 11:** Micro-tomography results compared with connected porosity,  $\phi_c$ , and permeability,  $k$   
 1219 (measured at a confining pressure of 0.7 MPa). Samples with higher  $\phi_c$  and  $k$  typically have  
 1220 higher mean pore volumes and mean throat areas, higher number densities of pores, throats  
 1221 and disconnected voids, a higher ratio of throats to pores per unit volume of analysed material  
 1222 (shown as ave. no. throats/pore), and a higher mean coordination number. Tortuosity  
 1223 decreases slightly with  $\phi_c$  but shows no consistent relationship with  $k$  in this sample set (blue  
 1224 indicates tortuosity in the x direction, purple in the y direction and red in the z direction).

1225

1226

1227



1229

1230 **Fig. 12:** Fitted curves (grey dashed lines) showing the relationships between key topological

1231 parameters (a–c) measured by micro-tomography. These relationships reflect the

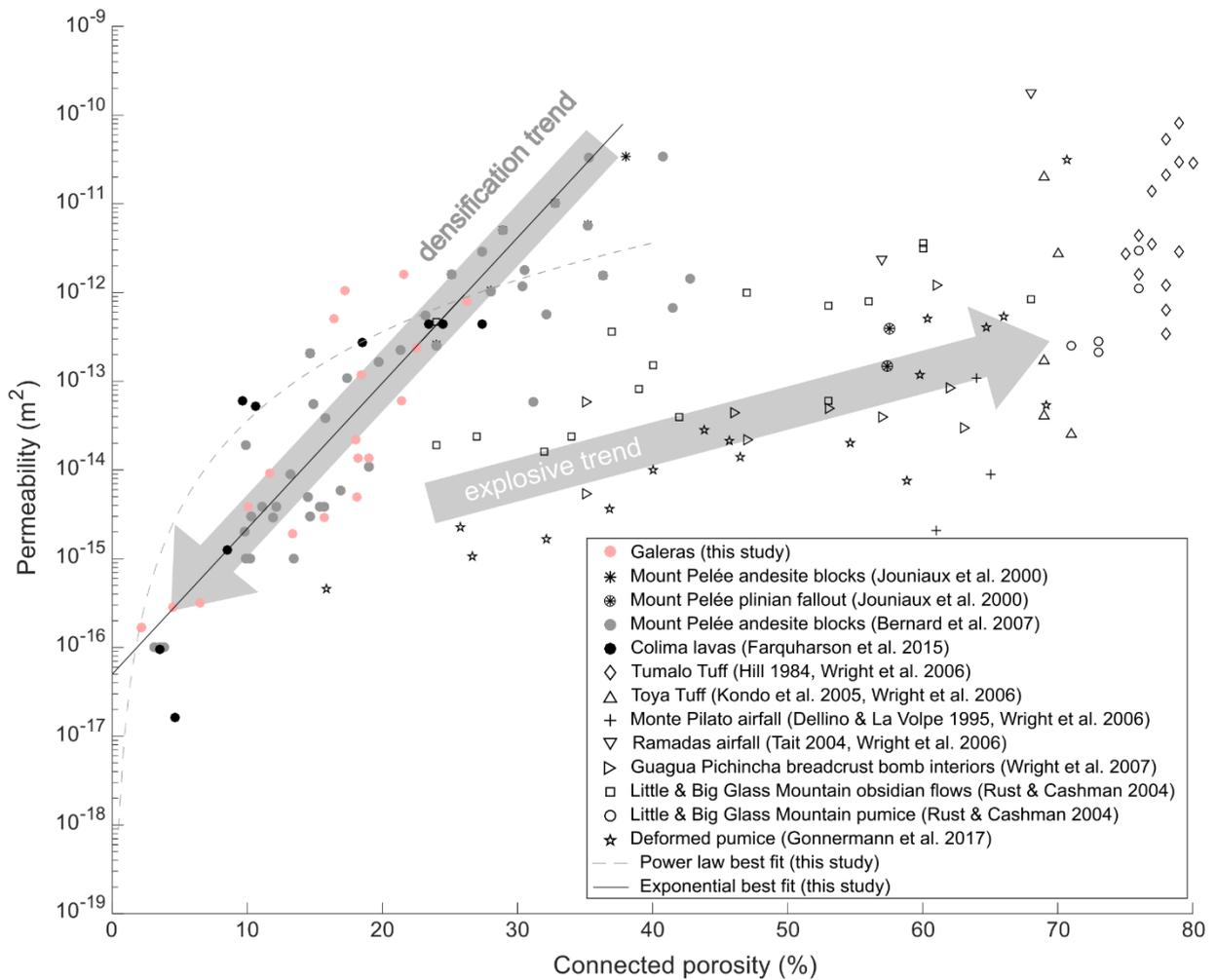
1232 densification process in the high-crystallinity andesites of Galeras volcano. Black filled

1233 symbols in panels b and c denote outliers that were excluded from the fitting procedure (see

1234 text).

1235

1236

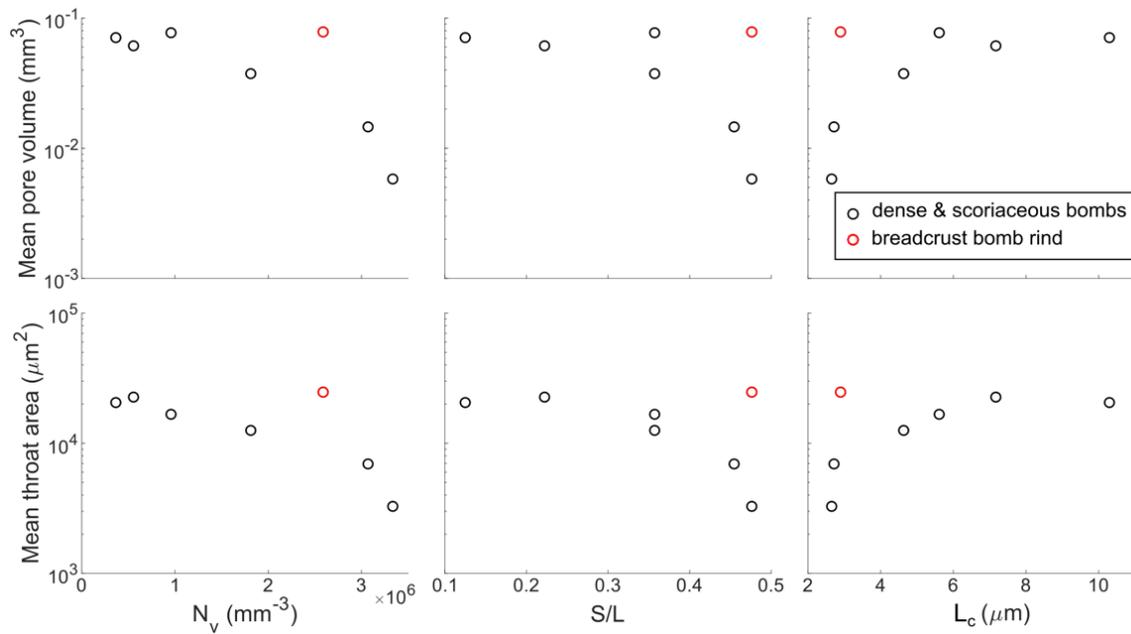


1237

1238 **Fig. 13:** Porosity and permeability (measured at a confining pressure of 1.4 MPa) data from  
 1239 this study plotted with data from selected effusive (filled symbols) and explosive (open  
 1240 symbols) volcanic products from published studies (see legend). The effusive samples shown  
 1241 here consist of lavas and blocks from block-and-ash flows from andesitic strato-volcanoes.  
 1242 Data from Galeras fit with the overall trend for these types of effusive products and show a  
 1243 higher permeability at lower connected porosities than explosive volcanic products, which  
 1244 follow a distinct trend. Also shown are the best-fit power law and exponential relationships  
 1245 for the Galeras data from this study (see section 4.2).

1246

1247



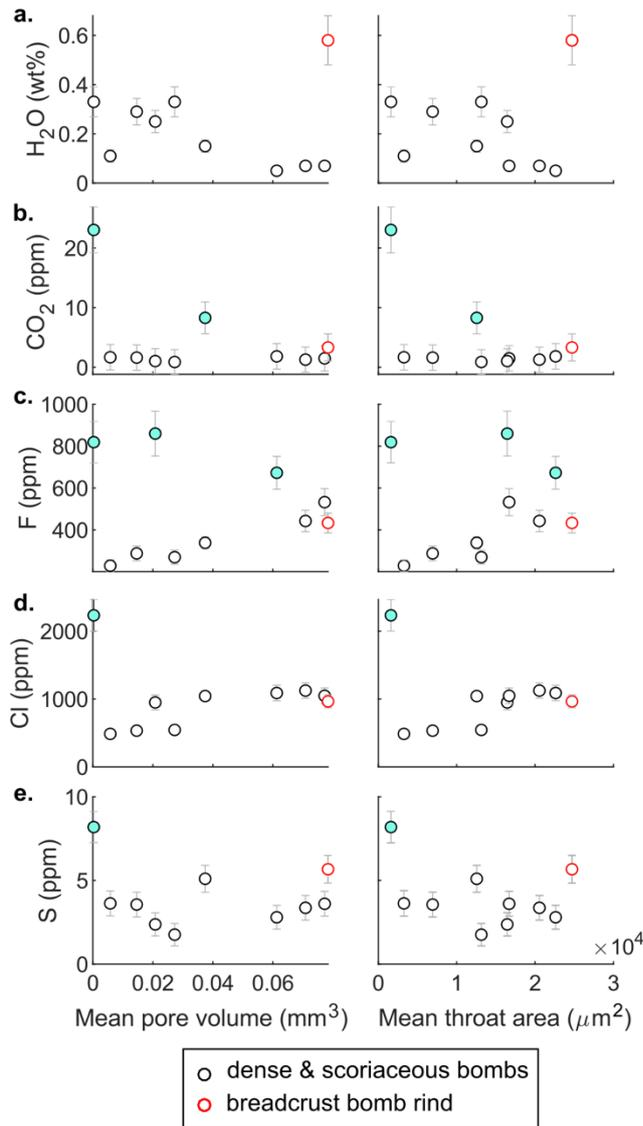
1248

1249 **Fig. 14:** Comparison of micro-tomography results with previously-published crystal micro-  
 1250 texture results for the same samples from the study of Bain et al. (2019).  $N_v$  is the plagioclase  
 1251 microlite volumetric number density calculated from crystal size distributions,  $S/L$  is the best  
 1252 fit plagioclase microlite aspect ratio (short axis / long axis) and the characteristic microlite  
 1253 size was calculated from the smallest size bins of the crystal size distributions. Samples with  
 1254 high  $N_v$ , high  $S/L$  and small characteristic microlite sizes have micro-textures characterised  
 1255 by high numbers of small, tabular microlites and show small mean pore volumes and mean  
 1256 throat areas. Samples with low  $N_v$ , low  $S/L$  and higher characteristic microlite sizes have  
 1257 micro-textures characterised by lower numbers of large prismatic microlites and show larger  
 1258 mean pore volumes and mean throat areas. The breadcrust bomb rind has the largest mean  
 1259 pore volume and mean throat area, and plots separately from the trend of the dense and  
 1260 scoriaceous bombs.

1261

1262

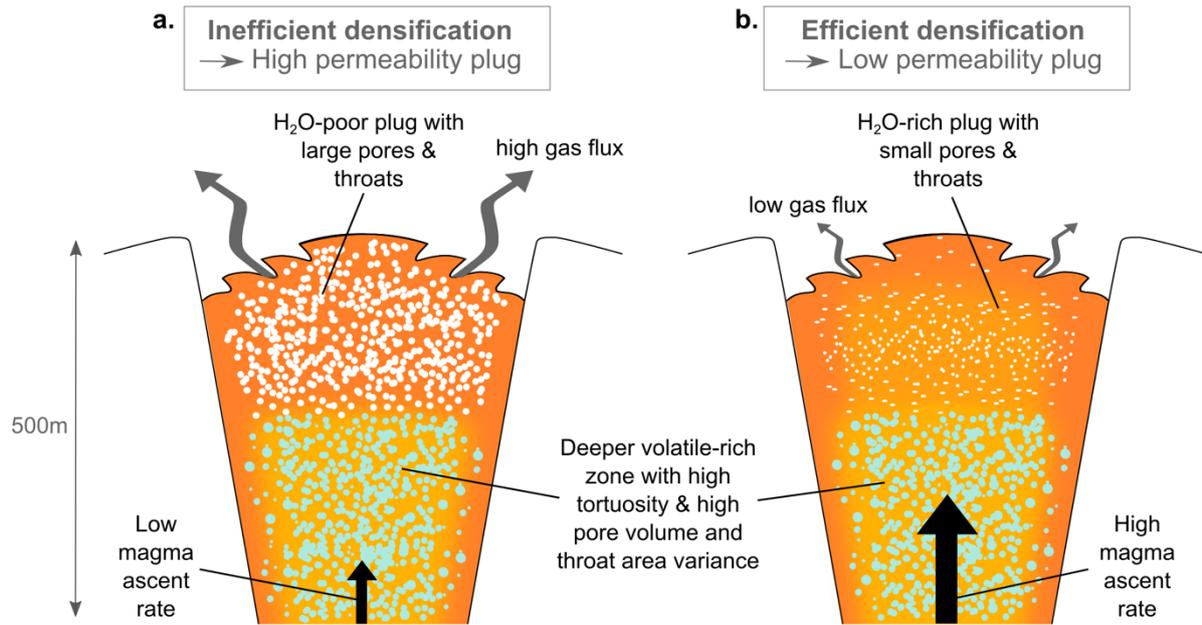
1263



1264

1265 **Fig. 15:** Comparison of micro-tomography results with previously published groundmass  
 1266 glass volatiles data for the same samples from the study of Bain et al. (2019), where vertical  
 1267 error bars correspond to two sigma. Horizontal error bars for the mean pore volume and mean  
 1268 throat areas are smaller than the symbol size. Outliers interpreted to result from the effects of  
 1269 vapour fluxing are coloured in blue (see section 5.4). Samples with the highest mean pore  
 1270 volumes and mean throat areas tend to have the lowest groundmass glass water content (H<sub>2</sub>O)  
 1271 but the highest Fluorine (F) and Chlorine (Cl) content, and vice versa. Carbon dioxide (CO<sub>2</sub>)  
 1272 and Sulphur (S) show no relationship with mean pore volume and mean throat area.

1273



1275

1276 **Fig. 16:** Conceptual model showing contrasting magma plug structures resulting from  
 1277 different densification efficiencies. **a.** Inefficient densification results from low average  
 1278 ascent and decompression rates, forming relatively high-permeability plugs with an H<sub>2</sub>O-poor  
 1279 residual melt phase. **b.** Efficient densification results from high average ascent and  
 1280 decompression rates, forming comparatively low-permeability plugs with a more H<sub>2</sub>O-rich  
 1281 residual melt phase.

1282

1283

1284

1285

1286

1287

1288

1289

1290 **Tables:**

1291

Sample name	Explosion date	Connected porosity $\phi_c$ (%)	Permeability $k$ (m <sup>2</sup> )	Micro-tomography	Crystal micro-textures <sup>1</sup>	Groundmass glass volatiles <sup>1</sup>
GAL1	2004-2010	4.5	$3.79 \times 10^{-16}$	-	-	-
GAL2	2004-2010	18.1	$6.48 \times 10^{-15}$	-	-	-
GAL3	2004-2010	22.5	$2.83 \times 10^{-13}$	-	-	-
GAL4	2004-2010	18	$1.72 \times 10^{-14}$	y	-	-
GAL5	2004-2010	2.1	$3.4 \times 10^{-16}$	y	-	-
GAL6	2004-2010	17.3	$1.08 \times 10^{-12}$	y	-	-
GAL7	2004-2010	13.3	$2.93 \times 10^{-15}$	y	-	-
GAL8	2004-2010	21.6	$1.63 \times 10^{-12}$	y	-	-
GAL9	2004-2010	18.2	$1.39 \times 10^{-14}$	-	-	-
GAL10	2004-2010	1.9	$1.13 \times 10^{-16}$	-	-	-
GAL11	2004-2010	15.7	$3.74 \times 10^{-15}$	-	-	-
GAL12	2004-2010	19	$1.25 \times 10^{-14}$	-	-	-
GAL13	2004-2010	18.4	$1.24 \times 10^{-13}$	-	-	-
GAL14	2004-2010	26.3	$8.95 \times 10^{-13}$	y	-	-
GAL15	2004-2010	6.5	$4.85 \times 10^{-16}$	-	-	-
GAL16	2004-2010	21.4	$6.98 \times 10^{-14}$	y	-	-
GAL17	2004-2010	11.6	$8.50 \times 10^{-15}$	-	-	-
GAL18	2004-2010	10	$4.51 \times 10^{-15}$	y	-	-
GAL19	2004-2010	16.4	$5.06 \times 10^{-13}$	-	-	-
AB2 <sub>T</sub>	11/12 Aug. 2004	-	-	y	-	-
AB8	12 July 2006	-	-	y	y	y
AB9	12 July 2006	-	-	y	y	y
AB14	17 Jan. 2008	-	-	y	y	y
AB15	17 Jan. 2008	-	-	y	y	y
AB16 <sub>bb</sub>	20 Feb. 2009	-	-	y	y	y
AB18	2 Jan. 2010	-	-	y	y	y
AB21	2 Jan. 2010	-	-	y	y	y
AB23	2004-2010	-	-	y	-	y
AB26	2004-2010	-	-	y	-	y
AB37	2004-2010	-	-	y	-	y

<sup>1</sup> Data from Bain et al. (2019). All other data from this study.

<sub>T</sub> indicates the tuffisite sample.

<sub>bb</sub> indicates the breadcrust bomb rind sample.

1292 **Table 1:** List of samples, connected porosity and permeability (measured at 0.7 MPa

1293 confining pressure) measurements and analyses performed. The complete permeability results

1294 are provided in Supplementary File B.

1295

1296

1297

Property	<b>GAL4</b>	<b>GAL6</b>	<b>GAL16</b>	<b>GAL8</b>
Connected porosity (%)	18	17.3	21.4	21.6
Permeability* (m <sup>2</sup> )	1.3-2.22 × 10 <sup>-14</sup>	1.03-1.08 × 10 <sup>-12</sup>	5.58-6.98 × 10 <sup>-14</sup>	1.55-1.63 × 10 <sup>-12</sup>
Mean coordination number	3.86	3.70	3.61	3.44
Number density of disconnected voids (mm <sup>-3</sup> )	17.7	17.2	5.8	6.6
Number density of pores (mm <sup>-3</sup> )	1.5	2.2	1.2	0.9
Number density of throats (mm <sup>-3</sup> )	4	5.3	3.2	1.8
Mean effective pore radius (μm)	77	117	173	154
Mean effective throat radius (μm)	27	48	60	60
Pore volume variance (mm <sup>6</sup> )	2.40 × 10 <sup>-2</sup>	5.73 × 10 <sup>-3</sup>	2.17 × 10 <sup>-2</sup>	1.45 × 10 <sup>-2</sup>
Throat area variance (μm <sup>4</sup> )	1.03 × 10 <sup>9</sup>	7.47 × 10 <sup>8</sup>	2.27 × 10 <sup>9</sup>	2.48 × 10 <sup>9</sup>
Tortuosity in x/y/z directions	n/a - n/a - n/a	2.36 - 2.58 - 2.18	2.73 - 3.45 - 3.05	2.34 - 3.99 - 2.02

\*Permeability measured over the range of confining pressures 0.7-2.1 MPa.

1299

1300 **Table 2:** Properties of the porous network in two low/high permeability sample pairs with  
1301 similar connected porosity (GAL4/GAL6 & GAL16/GAL8), calculated from micro-  
1302 tomography data.

1303